9-26-2017 2:00 PM

The Development and Numerical Modelling of a Representative Elemental Volume for Packed Sand

Ashraf Thabet, *The University of Western Ontario*

Recommended Citation

Abstract

The motivation of this thesis is the development of simple microscopic-scale model (representative elemental volume; REV) that can be used to conduct flow and heat transfer simulations from which closure coefficients can be established for the volume-averaged transport equations for porous media (packed bed). The thesis provides a brief introduction to the computational technique adopted for the geometric generation of the REV (YADE), followed by a parametric study undertaken to reveal the minimum number of particles inside the REV that are required to mimic the appropriate physics. Additional analysis was conducted with the goal of determining the influence of deviation in particle diameter. A wide range of particle temperatures was considered for analyzing the convective heat transfer and hydrodynamic behavior such the influence of property variation on temperature could also be studied.

The key research output is a detailed comparison of the results related to the hydrodynamics and heat transfer closures produced by an idealized, YADE-generated model against a three-dimensional, digitized model of packed sand. It is shown that the YADE model gives results that are in very good agreement with the digitized packed-sand model in the range of Reynolds numbers considered. The YADE model results were then compared with experimental findings and it was found that while the trends in convective heat transfer were well-predicted, there was a difference in the magnitude of the convective coefficients predicted and measured in previous experiments.

Keywords

Acknowledgments

I would like to thank my supervisor Dr. Anthony Straatman for his support, guidance, and advice with the encouragement to succeed.

I would like to thank OGS for providing me with the financial support to successfully conduct my research, and enhance my educational experience. Without your assistance, this project would not have been possible.

To my colleagues in the Computational Fluid Dynamics Lab, I am very grateful to have spent the last two years working with you and for the assistance you have provided me. This includes; Nolan Dyck and Mahmoud Elhalwagy. I am also thankful for the help of Marco Zanoni for providing the experimental results in addition to valuable advice and information, and Ian Molnar for the raw file of the digitized image.

Finally, I would like to sincerely thank my family and friends. Your support and encouragement has pushed me to realize my personal success.

Table of Contents

List of Tables

List of Figures

List of Appendices

Nomenclature

Latin Letter

a_{fs}	Specific interfacial surface area of porous media, m^{-1}
A_{fs}	Interfacial surface area of porous media, m^2
C_p	Specific heat capacity, J kg^{-1} K^{-1}
d	Particle diameter, m
L	length scale of porous medium or REV length, m
g	Acceleration of gravity, m s^{-2}
h_{fs}	Interstitial heat transfer coefficient between the solid and gas phases, W m^{-2} K^{-1}
k	Thermal conductivity, W m^{-1} K^{-1}
k_{fe}	Effective conductivity of fluid phase, W m^{-1} K^{-1}
k_{se}	Effective conductivity of solid phase, W m^{-1} K^{-1}
K	Permeability of the medium, m^2
C_E	Form drag coefficient for porous medium
P	Pressure, Pa
R	Specific gas constant of air, J kg^{-1} K^{-1}
v	Darcy velocity, m s^{-1}
u	Fluid velocity vector, m s^{-1}
U	Extrinsic velocity, m s^{-1}
amb	Ambient
m	Mass, kg
$\dot{m}$	Mass flow rate, kg s^{-1}
T_f	Temperature of fluid constituent of porous media
T_s	Temperature of solid constituent of porous media

T_p	Temperature of solid surface of particle in the packed bed
P_f	Fluid pressure
t	time
t_h	Heater on time
t_f	Final time
t_b	Blower time
Ra	Rayleigh number
Re	Reynolds number
Bi	Biot number
Pr	Prandtl number
$\mathbf{f}$	body force per unit mass, m s^{-2}
n	outward normal unit vector
$<>$	Denotes extrinsic volume-average
$<>^{f,s}$	Denotes intrinsic volume-average to constituent f or s
Greek symbols	
ρ	Density, kg m^{-3}
μ	Dynamic viscosity, Pa s
ν	Kinematic viscosity, m^2 s^{-1}
α	Thermal diffusivity, m^2 s^{-1}
$\phi\text{-}\varepsilon$	Porosity
σ	Stefan–Boltzmann constant, W m^{-2} K^{-4}
γ	Overall heat transfer efficiency, W m^{-2} K^{-1} Pa^{-1}
φ	Generic physical quantity
Δ	Denotes difference

Subscripts/superscript

avg	Average
cond	Conduction
conv	Convection
in	Inlet
out	Outlet
h	Heater
b	Blower
o	Initial
w	Wall
s	Solid
f	Fluid
eff	Effective
disp	dispersion
tor	tortuosity

Abbreviations

LTE	Local Thermal Equilibrium
LTNE	Local Thermal Non-Equilibrium
REV	Representative Element Volume
DEM	Discrete Element Method

Chapter 1

1   Introduction

This thesis presents an advanced physics knowledge in sequential steps. It starts with an introduction followed by a literature review of hydrodynamics and heat transfer closure in packed beds of sand. The microscopic and macroscopic scale of porous material is then discussed. The thesis highlights the background needed for building a project with the ultimate goal of developing a geometric model for packed bed of sand.

1.1   Background information about porous media

Fundamental and applied research related to heat and mass transfer in porous media has emphasized the significance of porous media in engineering applications. Growing interest in this area has resulted in a substantial increase in the number of related studies published in the literature. Significant progress has been made with respect to understanding the behaviour of fluid flow and mass movement in permeable porous media, including other important physical phenomena such as the exchange of energy and chemical reactions.

Porous media are heterogeneous materials composed of a solid microstructure (or matrix) and a fluid that fills the space unoccupied by the matrix. The structure and the material of the porous media play an important role in the physical behaviour of the media and in the interaction of the matrix with the fluid phase [1]. Considering their usefulness in applications including, for example, heat exchange, a full portrayal of their physical properties is necessary so that they can be adequately modelled in conjunction with other phenomena. The matrix can take a wide variety of forms, including packed beds of particles, networks of interconnected ligaments, or interconnected spherical voids.

The specific type of porous structure affects the way in which the fluid flows through the medium as well as the amount of the exposed internal area. For example, in enhanced heat transfer applications, it is preferable for the fluid to be able to pass through the matrix easily, but also to have a large amount of exposed internal area available for heat transfer.

The wide variety of porous media applications are the result of the wide range of properties exhibited by the materials. They can have very low conductivities for use in insulation or very high conductivities for heat transfer applications such as heat sinks.

Prior to a discussion of the scope of this work, the following brief introduction summarizes the most prominent developments in the understanding of porous media. The contributions made to the general understanding of transport in porous media can be categorized as either direct (e.g., Darcy and Carman) or indirect (e.g., Young and Fick).

The fundamental background reaches as far back as the 19th century. (In 1827 and 1845), the Navier-Stokes momentum equations were presented and then widely applied for the analysis of the hydrodynamics of porous media [2]. These equations are the foundation for the modelling and analysis of fluid motion. Later, in 1855, Fick's application law was introduced for approximating the relation between the concentration gradient and the diffusion flux applied in mass transport equations [3]. Another contribution was Darcy's empirical relation in 1856, which has been applied for flows through porous media when the Reynolds number based on the pore size or particle diameter is small [4]:

$$-\nabla P = \frac{\mu}{K}v \tag{1.1}$$

where P is the pressure, K is the permeability of the porous media, μ is the dynamic viscosity, and v is the vector of the average velocity.

Experimental evidence has demonstrated that, for numerous engineering applications, the operation of flows in porous media characterized by high Reynolds numbers, such as packed-bed reactors, is not fully described by Darcy's law. For this reason, to fit the experimental data, an additional nonlinear term, known as Forchheimer term, was introduced in 1901 in order to correct the of effect of inertia [5]

$$-\nabla P = \frac{\mu}{K}v + \frac{F\rho}{\sqrt{K}}v|v| \tag{1.2}$$

where ρ is the density. According to Ergun's study (1952), the Forchheimer coefficient F is given by $F = b/\sqrt{a\varepsilon^3}$, since a and b are constants that parameterize the microscopic geometry of the media [6].

Early in the last century, observations of simultaneous hydrodynamic dispersion and molecular diffusion were reported by Griffith [7,8]. In addition, the semi-heuristic Carman (1937) -Kozeny (1927) model of permeability described the permeability of packed beds reasonably well.

$$K = \frac{\varepsilon^3 \, d^2}{a(1-\varepsilon)^2} \tag{1.3}$$

where ε is the porosity of the porous media, d is the effective average diameter of a particle, and a is a constant for parameterizing the structure of the microscopic geometry of the porous materials and takes the value 180 for spheres [7,9]. Muskat later introduced a description of two-phase (one wetting and one nonwetting) flow in porous media by incorporating an effective assessment of permeability for each phase [4]. Brinkman's modification of Darcy's law and introduction of effective viscosity was published in 1948 [4]. Other early concepts include those presented by Gibbs' in 1878: his thermodynamic treatment of the interface between a liquid and its vapour included wetting phenomena, and the introduction of surface adsorption energy and entropy [10].

The first correlation of a totally effective thermal conductivity tensor for a two-phase flow in porous media was published by Weekman and Myers in 1965 [11] and a first semi-empirical interfacial (porous-plain media) boundary condition was studied by Beavers and Joseph in 1967 [12]. Constitutive equations for the diffusion of gases in porous media were developed by Mason et al. in 1967 and by Slattery in 1970 [4]. More recently, the closure of transport equations in porous media based on a volume-averaged method was derived by Whitaker in 1997 [13]. The latter form is the one most often applied in studies of porous media reported in literature [4]. (More information about the history of the exploration of porous media is provided in [4,7,9])

1.2 Heat transfer and hydrodynamics in porous media (volume-averaging)

Applications involving fluid flow and heat transfer in porous materials are encountered in numerous disciplines in science and engineering. For example, in chemical engineering, transport in porous media is related to filtering and drying applications, packed bed reactors, catalytic converters and fuel cells. In mechanical engineering, applications of porous materials include evaporative cooling, insulation and heat sinks. Moreover, porous media provide context for the study of groundwater flows and contaminant transport in groundwater in the environmental sciences.

An important environmental application of porous media is connected with smouldering combustion phenomenon. Smouldering combustion is characterized as an oxygen-limited flameless form of combustion with a slow propagation rate and a relatively low temperature. The phenomenon is extremely complex and includes heterogeneous chemical reactions and the transport of heat, mass, and momentum, including multiple phases [14]. Researchers have increasingly turned their attention to the study of this phenomenon with the goal of fully understanding and exploring the unknown mechanisms that characterize multiple chemical reactions, and heat and mass transfer processes.

Motivation of the study of smouldering combustion has arisen primarily from the possible economic and pollution-related impact of this phenomenon. In the USA, it has been reported that an estimated 31,200 smouldering fires that occurred during 2001 caused property losses of about US$400 million [14]. In Canada, since 1990, "wildland fires" have consumed an average of 2.5 million hectares a year, especially during prolonged periods of drought [15]. Such fires can smoulder underground all winter and then re-emerge at the surface in the spring. Figure 1.1 illustrates this effect.

Over the last decade, fire prevention costs in Canada have risen from about $500 million to $1 billion per year [15]. In China, subsurface fires caused by smouldering combustion account for 2% to 3% of the annual world emission of atmospheric CO_2. The statistics always lead to consideration of the economic damage and losses, which can pave the way to addressing the smoldering process through creative and preventive strategies that can
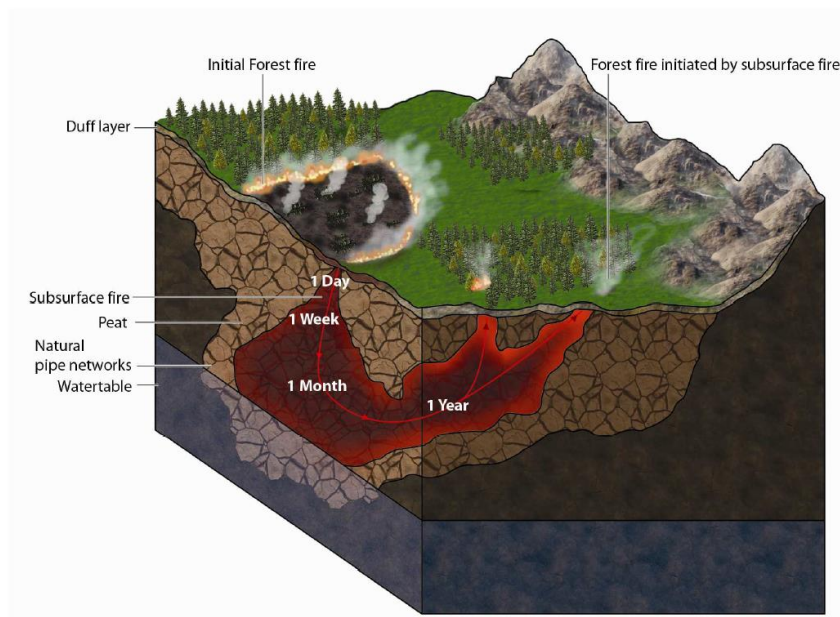
Figure 1.1: Image of a subsurface smouldering wildland fire. Fire initiated at the surface propagates in the ground and re-emerges months later [14].

also minimize their harmful effects on climate, the environment and human and animal life. A second aspect that attracts the attention of researchers is the feasibility of using smouldering combustion as a remediation technique. A recent new application called self-sustaining treatment for active remediation (STAR) has been developed based on in situ thermal technology derived from smouldering combustion. Compared to currently available techniques adapted for remediating groundwater and soil contamination, the new technology is distinguished by its potential to achieve technical effectiveness, the incorporation of a high rate of an instantaneous treatment, and the resultant substantial savings in operation and maintenance costs.

The source of fuel for this technology is the underground contaminants that are ignited and then oxidized using hot air, which is delivered through a well to the target zone. Following ignition and provided a sufficient amount of ambient or combustion air is supplied, the process is self-sustaining, without the need for external injected fuel [16]. Figure 1.2 portrays the principal components required for starting the STAR remediation process.
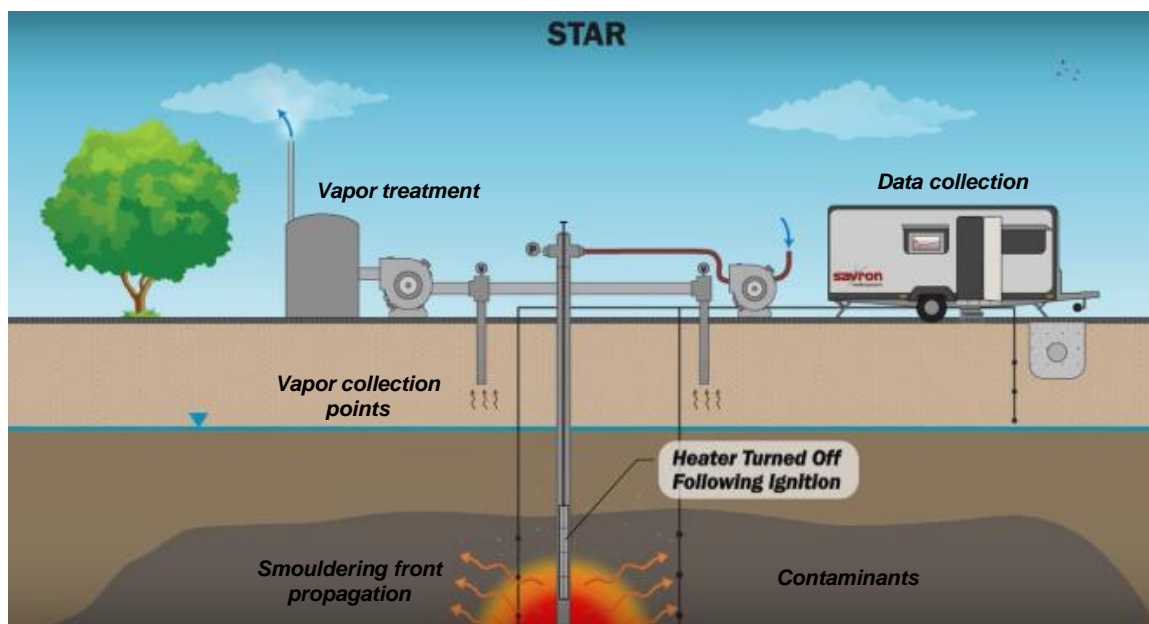
Figure 1.2: In situ treatment of contaminated soil. Schematic diagram of STAR components as a remediation solution [16] .

The relative complexity of analyzing and exploring smouldering combustion justifies further research targeted at acquiring a better understanding of the phenomena. Achieving this goal would ideally involve addressing and finding answers to important questions: What are the transport equations that describe the phenomenon in physical terms? Can the transport equations be simplified? What is the best discretization technique that should be adopted? It should be emphasized here that a set of mass, momentum, energy, species, and chemical reaction equations are required for describing the behaviour of a smouldering combustion system. Due to the high temperatures generated from the chemical reactions, local thermal non-equilibrium among the porous constituents must also be accounted for. Thus, the closure form for the interfacial heat transfer between the fluid and solid constituents of packed bed of sand was found to necessitate special treatment.

To answer the above questions, a model was constructed in an attempt to clarify the characterization steps inside a sample of a contaminated field (Figure 1.2). A portion of a contaminated porous media zone depicted in Fig. 1.3 is considered for analysis. Assume V_d is the space occupied by the porous medium with a length scale L, and let $V \subset V_d$ define the averaging volume having a length scale ℓ. However, V must be considered arbitrary

and large enough that the volume-average over a region is relatively insensitive to the particular choice of V, which is considered to be a representative elemental volume (REV) of the porous domain. The value of V must nevertheless be chosen small enough that $\ell \ll$ L, ensuring that the average of a quantity does not vary significantly within V and can be considered as a constant in integral terms. The latter assumption is adopted to guarantee the physical meaning of the averages in the model studied [13]. In this sense, a REV is a conceptual space unit, which is the minimum volume that can be located anywhere inside the porous medium (i.e., sand soil) within which measurable characteristics of the porous medium become continuum quantities [7].
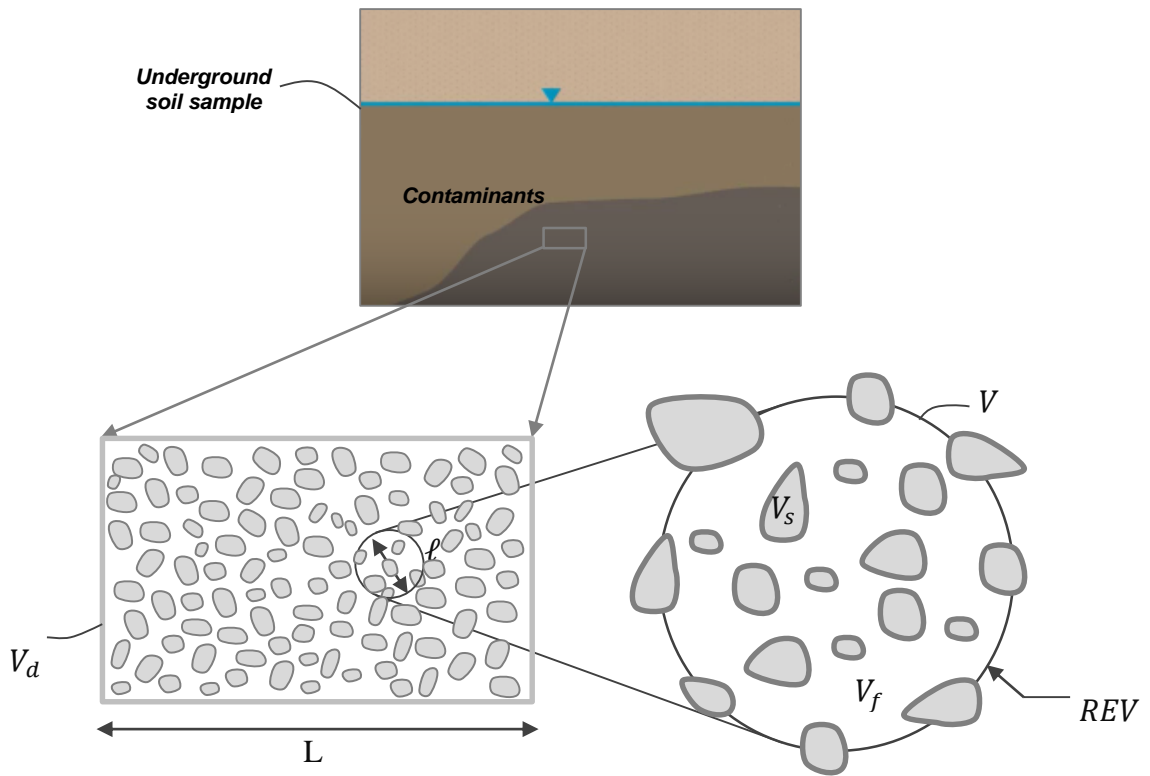
Figure 1.3: Illustration of an arbitrary porous medium containing fluid and solid volumes based on a volume-averaged method.

Two common approaches have been adopted for solving transport processes in the model mentioned above. In the first approach, the equations for the porous media are solved at the microscopic scale, which is characterized by the length scale of the particles. At this scale, the space between the particles is discretized, and the transport equations are applied

at their differential point and solved for the pore level forms. However, modelling the problem requires relatively large computational resources. For the second approach, the porous media can be treated as a continuum by adequately accounting for the role of each phase in the equations that define the transport through the system of phases. The REVs of the porous media are thereby scaled up to the macroscopic level, and the domain then consists of both solid and fluid phases characterized by the use of parameters such as porosity, permeability, and interfacial heat transfer to describe the transport through the domain.

To explain more effectively the behaviour of a fluid inside porous materials, researchers have adopted a variety of definitions of transport equations for describing the flow at the macroscopic scale within porous media. A strategy of volume-averaged is now considered the most appropriate technique for dealing with the behaviour of a fluid in porous media [17]. This refers to the fact that a volume-averaged model is derived based on the general transport conditions in the porous continuum. In this sense, it retains every required term, including those that identify the gradients of volume-averaging, which are difficult to frame in a traditional way.

The concept of a volume-averaging technique is that, for each element in the zone under study, a normal average over a volume can be characterized by joining the averages of an appropriate selection of points. Governing differentials that are transferred to volume-averaged equations represent a means of upscaling the equations in order to take into consideration the new arrangement of model behaviour so as to facilitate finding a solution for the bulk flow and thermal fields.

Because a volume-averaging discretization does not result in closure, breaking down the local transport variables according to those that are mainly volume-averaged and those that represent spatial deviation becomes essential. Based on this division, the outcome from the volume-averaging contains integral terms with spatial deviations that are related to the pore-level flow. Since the derived volume-averaged equations are solved for the bulk flow, spatial terms with deviation terms must be treated in a manner that seeks the final closure form of models studied. Chapter 3 provides a detailed information.

The acquisition of closure models for volume-averaged equations is usually accomplished using one of two methodologies. In the first, a semi-heuristic method replaces the pore-level terms with appropriately chosen terms involving volume-averaged quantities derived from empirical models. The second method entails the use of constitutive relations. In this case, variables of volume-averaged deviations are mapped onto the pore level field. The main reason for using pore-level solutions at that stage is to generate models for the different cases studied at the volume-averaged level.

In this sense, the semi-heuristic method suggested by Vafai and Tien [7,18] achieved closure for volume-averaged equations using well-known empirical relations. They summarized the deviation terms in the volume-averaged momentum equation in order to produce a body force term that acts on the fluid. This drag force is due to the interaction between the fluid and solid constituent and was modified to a higher form of Darcy's law. The proposed closure of the parameters for the momentum equation thus comprises the permeability and form drag coefficients. One of the important reasons for deriving the volume-averaged momentum equation is related to the presence of a viscous force between the layers of the bulk fluid. In cases in which this force is neglected, the model reduces to the well-known Darcy's law.

With respect to the energy equation, the same strategy is adopted as with the momentum equation. For example, Vafai and Tien [7] proposed a new effective heat flux vector characterized by an empirical effective conductivity term that includes an important bulk-scale thermal effect due to the impact of dispersion. This phenomenon is considered in the macroscopic volume-averaged bulk flow, representing the extra transport of thermal energy that is a result of pore-level mixing. This can be simplified as an enhanced mixing effect similar to the turbulent mixing phenomena. The effect of instability in a turbulent flow caused by both small and large eddies can be mapped in the same way when the irregular flow inside the structure of the porous medium is obvious. In this context, this effect should be considered, especially for flows with a high Péclet number, in which the impact of dispersion dominates by orders of magnitude compared to that of macroscopic conduction.

In this work, the primary consideration was the closure forms of the equations that express the conservation of energy and momentum in a packed bed of sand. These forms encapsulate the mutual effect between both solid and fluid constituents of porous media and should be thoroughly analyzed. For this reason, a complete analysis for different cases of REV geometries will be carried out.

The second goal of the research was to upscale the study toward a macroscopic (porous continuum) level. To this end, a one-dimensional column of packed bed of sand was employed to simulate an unsteady heat transfer case. In brief, this model is composed of an air diffuser and heater element placed at the bottom of a column of sand. The column measures about 0.505 m in height and 0.162 m in diameter. A portion of the packed-sand column is initially specified as a determined temperature to mimic electrical heating. An airflow is then imposed at the lower boundary of the column and the heating is stopped. Both conduction and convection are active in the column during this transient process, and thus the airflow causes a temperature pulse or wave to move through the column. Additional information about the computations and the experiment to which the computations are compared is provided in Chapter 5.

1.3   General objective and approach to the problem

The work presented in this thesis was motivated by recognition of the need for the modelling of transport equations in porous media at low Reynolds number. The focus of this work is the development of a simple microscopic (pore-level) geometric model that can be used for establishing the closure coefficients for a macroscopic (porous continuum) model. As the literature survey reveals, information about the hydrodynamic and thermal transfer in regions with low Reynolds numbers is lacking.

With respect to the pore-level scale, a brief introduction of the Computational Fluid Dynamics-Discrete Element Method (CFD-DEM) technique is given, followed by the development of a geometrically idealized packed-sand model developed using YADE. Detailed comparison of the YADE-based model is made to another model produced by digitization of a three-dimensional packed bed of sand [19]. The commercial software ANSYS-CFX is used to conduct pore-level simulations of flow and heat transfer in these

models. A parametric study is presented to establish the minimum required number of particles inside the REV, the influence of deviation in particle diameter and the effect of the temperature variation on the results. Chapter 4 provides additional details.

At the macroscopic (porous continuum) level, a model based on the non-equilibrium volume-averaged transport equations is presented. Volume-averaged models have proven to be a powerful method of modelling flow in porous media, however the derivation of the closure form of these equations must be treated carefully to ensure accurate results. Semi-heuristic closure models are presented herein, in which unknown terms are replaced with heuristic models that mimic the aggregate processes on a volume-averaged scale. Closure coefficients in these heuristic models, such as permeability and interfacial heat transfer, are established from the pore-level computations on the REV models described above. The volume-averaged equations are then solved for a one-dimensional case of a packed bed of sand for a comparison with the results presented in [20].

1.4 Thesis outline

The following chapters in this thesis outline the framework for modelling and analyzing transport in porous media with complex porous domain geometries and the application of a volume-averaged method in a relevant application of packed beds of sand.

The contents of the chapters are as follows:

- Chapter 2:

  Provides a brief review of the literature related to smouldering combustion, the discretization method used for transport equations, and the microscopic closure of transport equations for packed beds of spheres including the REV development for pore-level study. The review highlights the work that has already been conducted as well as knowledge gaps that remain.

- Chapter 3:

  Describes the derivation of the volume-averaged model used for simulating heat exchange between air and sand in a packed bed based. The model incorporates the local thermal non-equilibrium (LTNE) approach.

- Chapter 4:

  Presents pore-level simulations on the YADE and digital REVs for the purpose of comparing the two geometric models. The application of CFD-DEM technique based on YADE software [21] in order to generate REVs is detailed along with parametric study of the REVs.

- Chapter 5:

  Outlines the solution of the volume-averaged transport equations as a means of comparing the numerical model results with experimental ones. The effects of the generated correlation on the experiment of sand column are examined, and the simulation results that prove the validity of the developed model are presented and discussed.

- Chapter 6:

  Summarizes the work and its contributions, and lists recommendations for future work.

Chapter 2

2   Literature Review

This chapter provides a review of the literature related to smouldering combustion, the modelling of porous media, and packed beds of particles. The scope of the work undertaken for this thesis is also explained. With the goal of examining the smouldering combustion phenomenon as a pathway to soil remediation, it was determined that a brief survey of this field would provide a global picture that would help advance progress toward a final robust model and that knowledge of the most recent progress reported in the literature would enrich and enhance an understanding of this phenomenon. Following this brief survey, the literature related to the porous media was explored, and the most suitable governing and discretization method was investigated in an effort to identify the most accurate numerical model. The results of these areas of the literature review are provided here, along with discussion of packed bed of spheres (sand) as a matrix of porous media, including details of REV development for pore-level study and cases involving the most popular correlations between fluid and solid constituents.

2.1   Smouldering in porous media

Smouldering is generally classified as either forward smouldering in which the reaction zone propagates in the same direction as the oxidizer flow, or opposed smouldering in which the reaction zone propagates in a direction that opposes that of the oxidizer flow (Figure 2.1). Opposed smouldering is considered a more common fire initiation scenario [22]. In the literature, forward smouldering has received relatively little attention, although a number of experimental and theoretical studies can be found that address multiple scenarios. Schult et al. [23] employed asymptotic methods for investigating smouldering wave solutions that have two different structures: a reaction leading wave structure, when the velocity of the combustion layer exceeds that of the heat transfer layer, and a reaction trailing wave structure produced when the combustion layer is slower than the heat transfer layer. A reaction leading wave structure occurs when the incoming oxygen concentration is sufficiently high. Their experiments provided qualitative theoretical descriptions of a
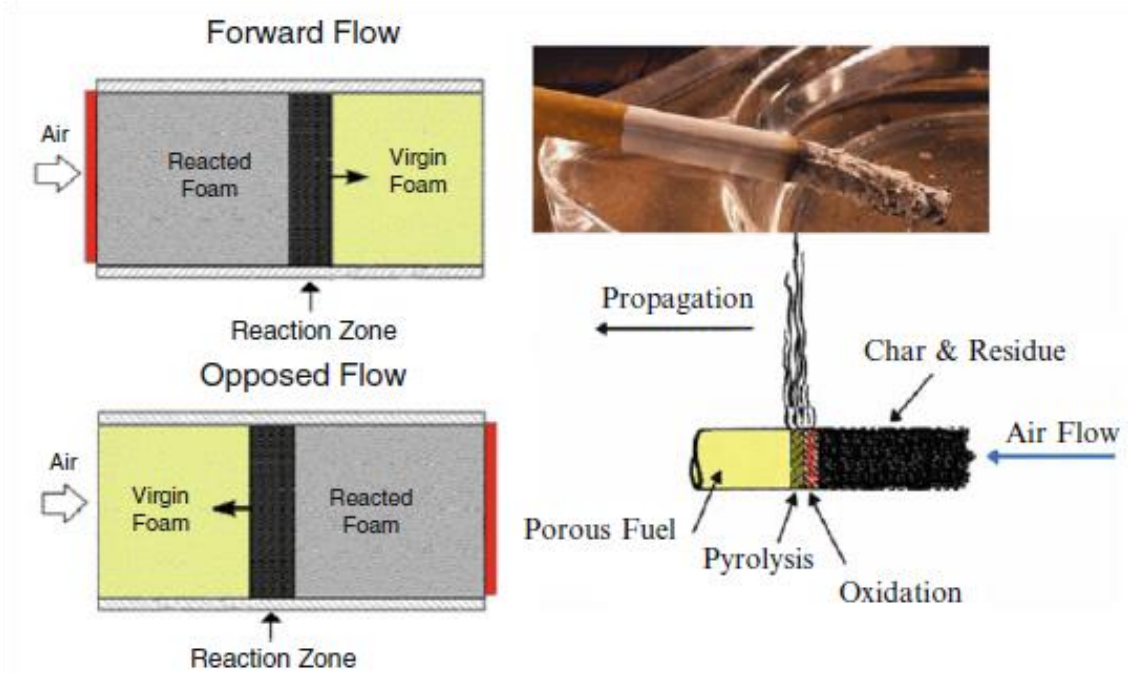
Figure 2.1: Forward and opposed types of smouldering. Airflow direction versus the smouldering combustion propagation [14].

variety of experimental observations of forward smouldering; however, in their modelling, they assumed a local temperature equilibrium. Leach et al. [22] developed an advanced model based on local chemical and temperature non-equilibrium between a solid and a gas, although they neglected the pressure drop across the pile, which meant that the conservation of momentum equation was not solved.

Ohlemiller presented independent energy equations for the gas and solid phases based on the smouldering of cellulose [24]. With respect to forward smouldering, Summerfield et al. [25] also assumed a thermal non-equilibrium. Fatehi and Kaviany [26] incorporated some forms of chemical non-equilibrium in their examination of reverse smouldering. Chen et al. [27] recently implemented a new one-dimensional model that considers the drying process and the mass transfer mechanism of vapour. They took into account the boundary layer effect on oxygen diffusion process, which influences the combustion rate. However, a local thermal equilibrium and only one kinetic reaction were assumed. Fang et al. had previously solved the same model numerically assuming only two elements, char and ash, as a reactant and product, respectively [28]. One drawback associated with these

earlier one-dimensional simulations of smouldering combustion is that they cannot directly model the heat loss to the external environment in the perpendicular direction, as occurs in actual experiments [29]. Most previous studies modelled solid materials (porous matrix) exclusively. In contrast, no numerical investigations of a non-aqueous phase liquid (NAPL) as a fraction of the fluid constituent of porous media have been reported in the literature. A few recent attempts have been made to track a smouldering front, but these studies began to appear few years ago.

It was evident that appropriate modelling of the smouldering combustion phenomenon in porous media necessitated the building of a mathematical model of the corresponding physical properties associated with correct assumptions, followed by the development of an appropriate numerical model.

2.2   Modelling porous media

In general, porous media applications are widespread in the areas of chemical, environmental, mechanical and petroleum engineering. Such applications involve porous media of varied types and characteristic lengths. Examples include catalytic and inert packed bed reactors, contamination migration in groundwater, single and two-phase transpiration cooling, and enhanced oil production [4].

Porous media are generally heterogeneous materials that involve a solid structure framework and a fluid that fills the surrounding space. Of particular interest are applications involving heat transfer in porous media, in which the connectivity of the interconnected pore structure allows the fluid to penetrate around the solid constituent of the porous matrix. For example, literature reports commonly discuss a cooling application, whereby a cold fluid passing through a porous matrix removes a significant amount of heat generated at the hot surface of the solid constituent to which the porous material is connected [4,30]. The mechanism involved is similar to that in traditional heat sinks; however, the effective surface area in the porous materials is often several orders of magnitude greater [4]. It was found that the larger the exposed surface area of the solid constituent, the more heat transfer energy can be extracted, which means that multiple solutions of complex applications are available in many heat transfer cases. In other

applications, rather than only a sensible heat mechanism being addressed, latent heat is also considered, provided phase change occurs.

For accurate estimates of heat and mass transfer, complete description of the physical properties of the porous materials are essential. For this reason, a goal of the work conducted for this thesis was to explore the heat transfer phenomenon at low Reynolds numbers for randomly packed beds of sand and this is an area that is currently weak with respect to the modelling of smouldering.

The prediction of flow characteristics in porous media has been a topic of study for more than a century. As previously mentioned, a notable discovery in this area originated with Darcy, who was able to relate a drop in pressure to bulk velocity using an empirical constant. Darcy's law is given as

$$\frac{\Delta P}{L} = -\frac{\mu}{K}v \qquad (2.1)$$

where ΔP is the pressure difference across the length L.

The Darcy's law equation expresses a linear relation between pressure and bulk velocity and that is valid only in viscous dominated flows, where the Reynolds number is low. For convective dominant flow, this equation is no longer valid and more advanced correlations are needed. The correlated term in this expression is the permeability, and as given in Eq. 2.1, this parameter is a measure of the resistance of the porous material to the fluid that flows through it.

The Darcy equation alone is not valid for Reynolds numbers greater than ten, and an alternative correlation is needed for accurately modelling the effect of a porous structure on a flow (Figure 2.2) [31]. Ergun built an expression based on consideration of granular solids, which is suitable for addressing higher Reynolds numbers by taking into account both the porous matrix and the particles. Ergun's equation contains a linear term similar to the Darcy's law equation, plus a quadratic term that accounts for the effects of inertia, but is limited to porous media having a specific internal structure. For more advanced work, Ward succeeded in upgrading the correlation based on other information about the internal

structure: he used dimensional analysis to show that the quadratic term in Ergun's equation could be represented in terms of the dynamic pressure, the square-root of the permeability, and a drag coefficient [32]. The new expression is known as a form drag.

The volume-averaging method, developed independently by both Whitaker [33] and Slattery [34], is a method for modelling flow and energy transport in porous media. These transport equations are applicable in complicated regions, because they are developed from the transport equations for a single constituent continuum and therefore contain all relevant terms that resolve the gradients. The idea behind this method is to solve transport equations that are integrated over a representative volume, resolving the bulk flow. This method can also be extended to all transport equations, such as those for mass fraction and thermal fields, for which Whitaker used volume-averaging in order to find closure for the physical processes [13]. It is important to note that volume-averaging does not primarily present a closed form of transport equations; instead, it contains integral terms based on the microscopic level. Consequently, at the macroscopic level, the bulk flow solution must provide these terms. It has been stated that a closure form can be achieved by either of two methods: 1) the use of constitutive equations when an examination of flow at the pore scale
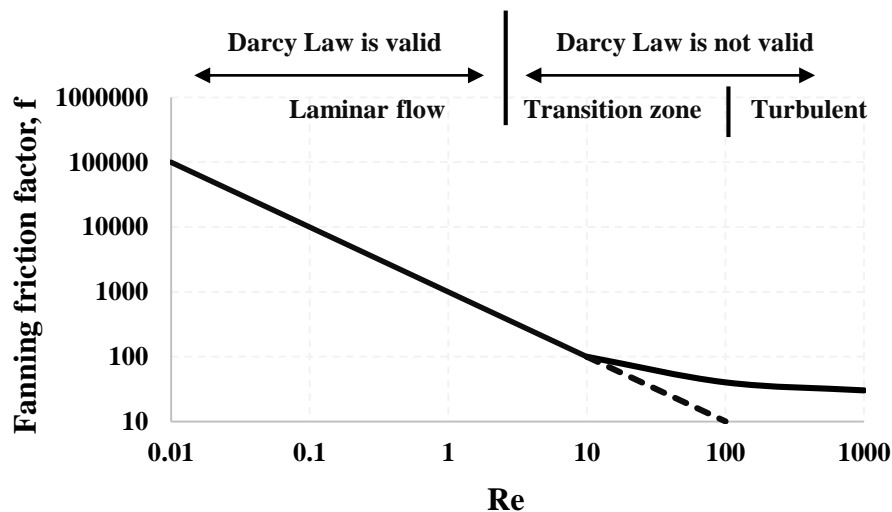
Figure 2.2: Schematic of the classification of flows through porous media [31].
Reproduced Data.

is needed and 2) a semi-heuristic method that replaces the integral terms with terms that relate to the volume-averaged parameters often derived from empirical relations such as the Darcy or Ergun equations in the momentum equation. This work uses a semi-heuristic form of closure to represent the final form of the volume-averaged equations.

2.3   Packed beds of particles

A packed bed is a heterogeneous system composed of solid particles and a fluid flowing in the interstitial space among the particles. Because of its heterogeneity and complexity, a packed bed has not been the subject of exact, fully detailed simulation theory. However, instead of an exact theory, a rather conventional and more realistic approach has often been employed. A typical example is the assumption that a packed bed can be treated as a series of mixing cells with multiple particles in each cell. This idea governs the volume-averaging of a packed bed of particles.

Over the past four decades, a series of articles has been published concerning the decrease in particle-to-fluid heat and mass transfer coefficients with a decreasing flow rate at a low Reynolds number. In fact, this behaviour had been observed experimentally by a number of investigators, each of whom arrived at different correlations. The importance of careful analysis in the work presented in this thesis was thus evident.

The goal of studying a representative element volume (REV) for a packed bed at the microscopic scale is to eliminate the necessity of modelling the problem at the full scale of the particles, thus clearly and significantly reducing the computational time required. However, using this approach requires that detailed information about the pore-level structure and flow field be determined and provided via physical models that characterize the porous region [35].

The approach of developing a REV for pore-level study has been used recently in heat transfer enhancement studies using porous media. Yu et al. proposed a unit-cube geometry model that is based on interconnected sphere-centered cubes, called unit-cube in order to characterize the internal structure of graphitic foam, [36] (See Fig. 2.3). They studied the heat transfer and fluid flow in porous carbon foam. Another improvement came from

Karimian and Straatman [37]. They derived a semi-heuristic closures based on the simulation results of heat transfer and hydrostatics in unit cubic.

a)   **b)**
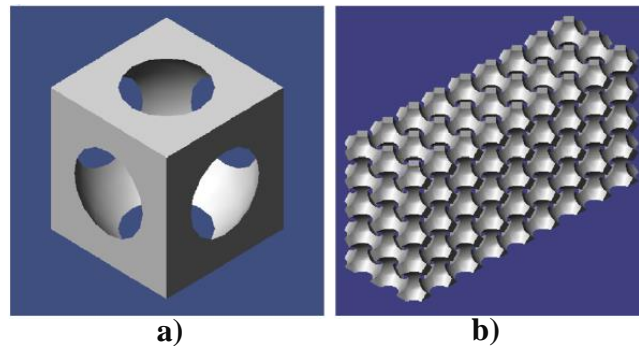
Figure 2.3: CAD images showing the unit-cube model. (a) A single unit-cube with spherical void, and (b) A pore block containing interconnected pores [37].

Another study of a simple cubic packing, shown in Fig. 2.4, has been used to build a channel of large number of particles [38,39]. As a result, heat transfer and pressure drop have been studied in a structured packed bed. They conducted different experiments, studied the forced convective heat transfer in order to generate a heat transfer correlation, and finally compared their results to other studies. More recently, researchers have increasingly turned their attention to the idea of building beds of randomly-packed particles numerically-generated that are based on different shapes and assumptions.
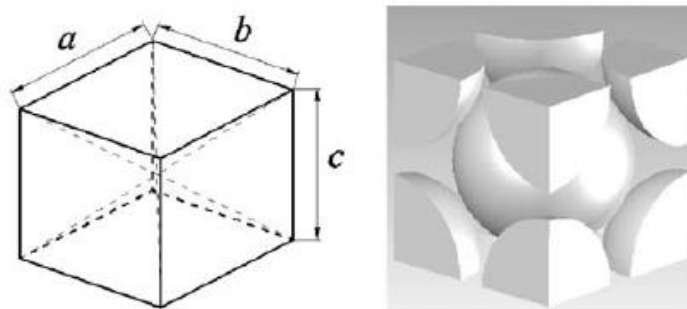
Figure 2.4: Cubic box and spheres for simple cubic packing [38].

Fluid-to-particle heat transfer correlation received extensive attention in the last century, primarily during the 1970s. These empirical correlations showed that the heat transfer coefficient is dependent on the porosity, particle size, and shape of the packed bed as well

as on the Prandtl number of the fluid and the Reynolds number derived from the range of the particle diameters [7].

Dimensionless analysis of the problem suggests that the thermal boundary layer of the particles surrounded by a fluid at a specific temperature is a reflection of the dynamic boundary layer. A more general correlation can be suggested, as follows:

$$\text{Nu} = a + c\, Pr^m Re^n \tag{2.2}$$

where Nu is the Nusselt number [30], and $a, c, m,$ and n are unknowns that require closure for the conditions under consideration. In 1979, Wakao et al. published their well-known correlation for packed bed of spheres, wherein the experimental data varied between $0.7 < Pr < 1$ and $15 < Re < 8500$, and the particle diameters were of the order of 10 mm to 130 mm [7,40].

$$\text{Nu} = \frac{h_{sf} d}{k_f} = 2 + 1.1\, Pr^{1/3} Re^{0.6} \tag{2.3}$$

This correlation has been widely used in the studies of packed bed reported in the literature. In this regard, it could be extended with certain margin of error to include consideration of low Reynolds numbers or of particles with small diameters or geometric shapes other than spheres. In 1982, Kar and Dybbs [41] developed another correlation

$$\text{Nu} = 0.004 \left(\frac{d_v}{d_p}\right)^{0.35} Pr^{1/3} Re^{1.35} \tag{2.4}$$

where $d_v = 4\varepsilon/a_{sf}$ is the average void diameter, and d_p is the particle diameter. This correlation is valid for $Re < 75$, but it underestimates the interfacial heat transfer at low Reynolds numbers. In the literature, different categories of correction for turbulent and laminar zones, structured and unstructured particles, and foam and packed beds have been employed to characterize the final formula. In this respect, it is common to have different formulas such that the coefficient a of Eq. 2.2 is nullified for cellular materials [42]:

$$\text{Nu} = 0.124\, (RePr)^{0.791} \tag{2.5}$$

Another option is for the second term $Pr^m Re^n$ of the same equation to be multiplied by the porosity (ε) for spherical particles whose porosity is within the range of $0.7 < \varepsilon < 0.95$ [43].

$$\text{Nu} = 0.07 \left(\frac{\varepsilon}{1 - \varepsilon}\right)^{2/3} (RePr) \tag{2.6}$$

The studies published in the literature are significantly lacking in information beyond some specific zones of Reynolds and Prandtl numbers. Figure 2.5 depicts this distribution of the available data, which highlights the necessity of filling the knowledge gap. It is clear that between Prandtl (Pr) or Schmidt (Sc) numbers of 1 and 120, no details concerning heat or mass transfer behavior are available. The Prandtl number is the ratio of the kinematic viscosity (also referred to as the momentum diffusivity), ν, to the thermal diffusivity α. It provides a measure of the relative effectiveness of momentum and energy transport by diffusion in the velocity and thermal boundary layers, respectively [30]:

$$\text{Pr} = \frac{\nu}{\alpha} \tag{2.7}$$

The Schmidt number is the ratio of the momentum diffusivity, ν, and the mass diffusivity, D. It provides a measure of the relative effectiveness of momentum and mass transport by diffusion in the velocity and concentration boundary layers, respectively [30]:

$$\text{Sc} = \frac{\nu}{D} \tag{2.8}$$

For Reynolds number less than 20, a small amount of information is available and is associated with a high degree of uncertainty. Figure 2.6 provides a graph representing the well-known correlation developed by Wakao et al. as in Eq. 2.3. The figure includes the results of a variety of experiments based on multiple assumptions about unstructured packed beds of particles. Recently, a new study based on experimental analysis described the heat transfer for small size of particles and a correlation has been developed as [20]

$$\text{Nu} = 0.001 \, Re^{1.97} \, Pr^{1/3} \tag{2.9}$$

It must be noted that although the flow and heat transfer performance of randomly packed beds might not be optimal, the pressure drops in such packed beds are considerably higher
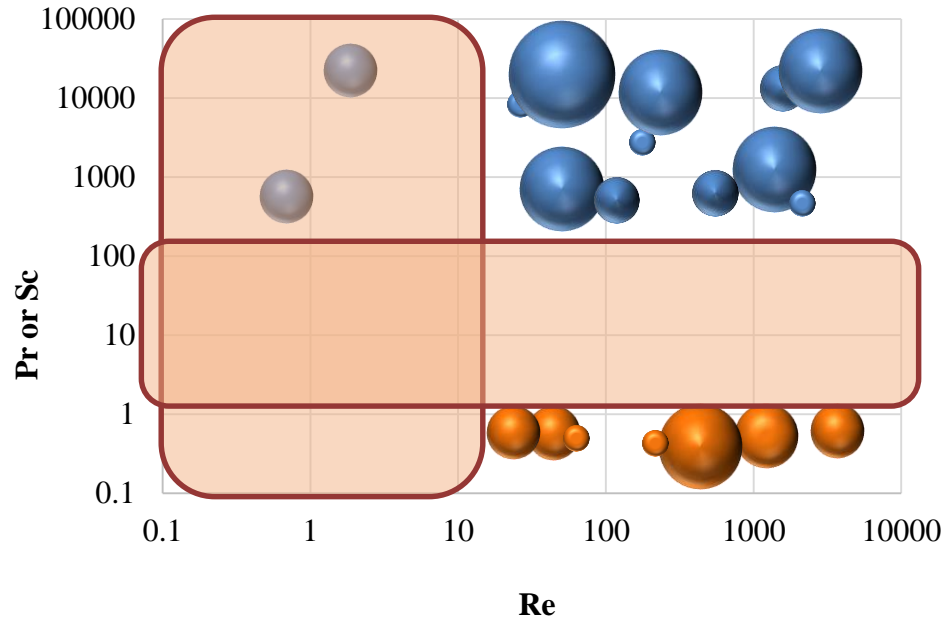
Figure 2.5: Approximate schematic of ranges of dimensionless numbers covered by experiments reviewed and reported in Wakao and Kaguei [44].
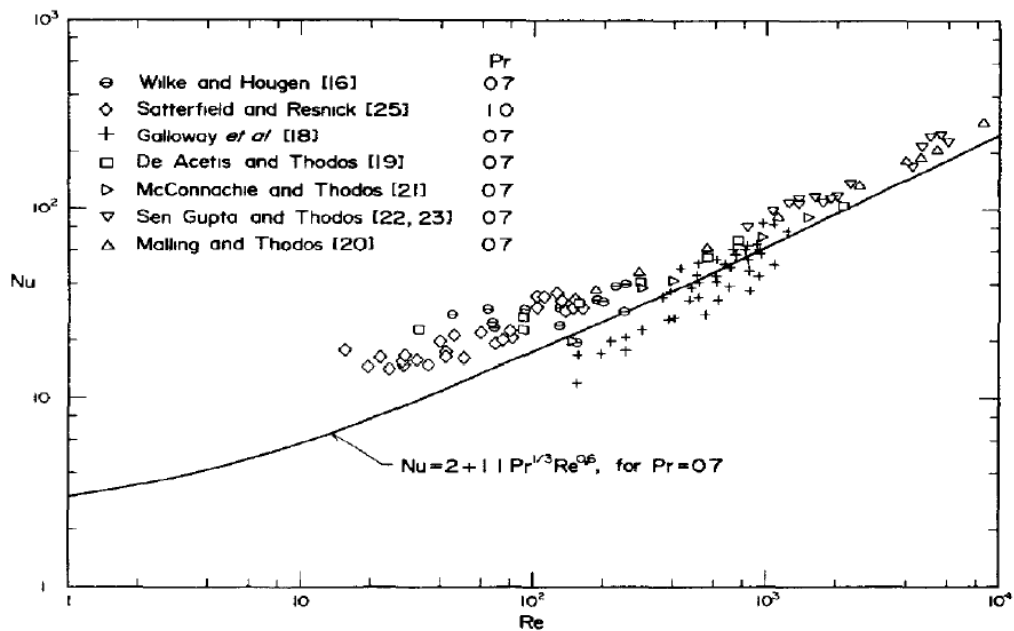
Figure 2.6: Heat transfer data from steady-state experiments [40].

than those in other forms of packed beds [39], which can significantly lower the overall heat transfer performance. One remedy for this effect is to construct a structured packed

bed of particles, thereby achieving a notable reduction in the pressure drop and observable improvement in heat transfer performance.

Researchers have studied the relation governing heat transfer between the fluidizing gas and the bed of particles. Coefficients for the entire bed have been evaluated through the use of different types of experiments conducted in order to test steady state and unsteady state techniques.

In Fig. 2.7, it can be seen that for $Re_p > 100$, the Nusselt numbers fall between the values for single particle and those for fixed beds [45]. For $Re_p < 10$, the Nusselt number decreases drastically when the Re_p decreases and has values far smaller than one. In the region of a rapidly falling Nusselt number, the empirical expression of Kothari [46] fits all of the reported data; thus

$$\text{Nu} = 0.03\left(Re_p\right)^{1.3} \quad 0.1 > Re_p > 100 \tag{2.10}$$

2.4 Project scope and summary

The goal of this work was to complete a study of (spherical-phase) packed bed of sand in order to address the gap evident in the literature with respect to low Reynolds numbers. Achieving this goal entailed the creation of a general three-dimensional REV to be used for obtaining the physical parameters of an arbitrary pore geometry. Analyzing transport equations in porous media with multiple shapes of particles (porous domain geometries) was then developed. The following specific steps in this overall goal were identified:

- Construct a geometric model to represent at a microscopic level the corresponding physical problem, along with appropriate assumptions.
- Derive the closure form for the volume-averaged momentum and energy equations in order to characterize the effective properties of porous media.
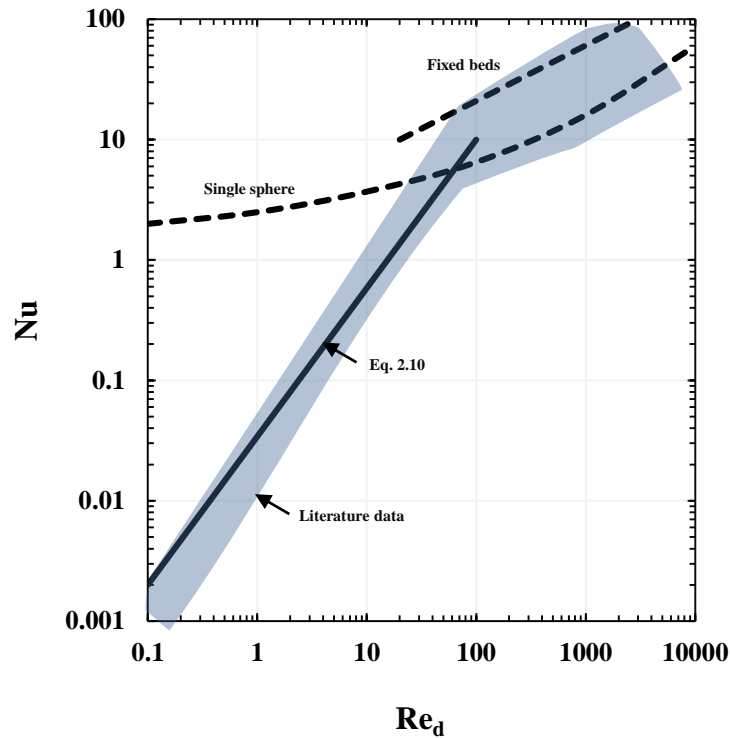
Figure 2.7: Data from the published literature: Shaded area represents the experimental findings of 22 studies [45]. Reproduced Data.

- Develop a suitable numerical model for computing fluid flow and heat transport in porous media based on the finite-volume method, which incorporates robust and accurate conditions that are effective for different flow speeds.

As stated earlier, an additional goal of this work was to extend the capability of an in-house code to include unsteady conduction/convection heat transfer at a high temperature level so that applications such as heat transfer combustion and two-phase reactions in packed beds of particles can be simulated. Solving the fluid flow transport equations required the unit-cell structure of porous media for which a finite volume approach was adopted similar to that used by Betchen et al. [47].

Chapter 3

3 Transport Equations in Porous Media

In this chapter, we start by defining the general pore level transport equations followed by the volume-averaged technique applied in the macroscale of porous media. Afterwards, we introduce the closure forms for both the momentum and energy equations for fluid and solid constituents. All assumptions needed to close the energy equations based on local thermal non-equilibrium method are shown later.

3.1 Pore-level (Microscopic) governing equations

At the pore-level scale, the flow and thermal behaviour is described by the standard mass, momentum, and energy conservation equations. The mass and momentum equations for an incompressible, Newtonian fluid with constant properties are given by

$$\nabla.\mathrm{u} = 0 \tag{3.1}$$

and

$$\rho_f \left(\frac{\partial u}{\partial t} + \mathrm{u}.\nabla\mathrm{u} \right) = -\nabla\mathrm{p} + \mu_f \nabla^2 u \tag{3.2}$$

Under the same assumption, the energy equations for the fluid and solid phases are given as

$$\rho_f c_{p,f} \left(\frac{\partial T_f}{\partial t} + \mathrm{u}.\nabla T_f \right) = k_f \nabla^2 T_f \tag{3.3}$$

and

$$\rho_s c_{p,s} \frac{\partial T_s}{\partial t} = k_s \nabla^2 T_s \tag{3.4}$$

Eqs. 3.1-3.4 are used to compute the pore-level flow and temperature fields, and are the starting point from which the volume-averaged equations are to be derived. It was also assumed that viscous dissipation in the fluid phase is neglected.

3.2 Volume-averaging energy equations

The following assumptions are considered:

   I.   Transient flow.
  II.   Laminar and incompressible flow.
 III.   Uniform properties and porosity of porous media.
 IV.   The local thermal non-equilibrium (LTNE) method.

3.2.1   Mass and Momentum

The local volume-averaging study of problems involving heat and/or mass transfer, and chemical reactions in porous media requires the treatment of fluid flow, mass and heat transfer simultaneously. In most cases, the concept of local thermal non-equilibrium is assumed in the heat and mass transfer equations. Figure 3.1 shows various possible types of thermal transport inside a REV [13,48].
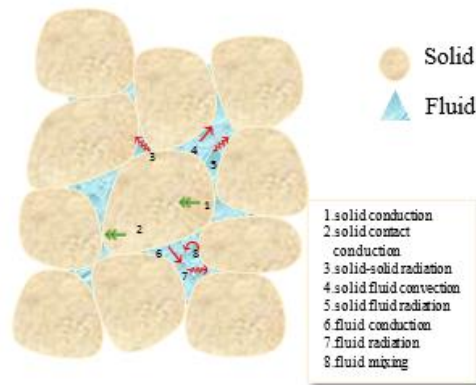
Figure 3.1: Possible modes of heat transfer in porous media.

In the porous continuum region, volume-averaged forms of the transport equations are used. In this context, transport equations are integrated over a representative elemental volume (REV) of a porous media. Volume-averaging integration is adopted at the studied zone, where there exists a volume-averaged value of a quantity $\langle \varphi_f \rangle$ defined by the following expression:

$$\langle \varphi_f \rangle = \frac{1}{V} \int_{V_f} \varphi_f \; dV \tag{3.5}$$

where, V is the volume over which the averaging is carried out, V_f is the fluid volume inside V, and $\langle \varphi_f \rangle$ is the extrinsic-averaged (superficial) quantity of φ_f. Similarly, an intrinsic-averaged quantity $\langle \varphi_f \rangle^f$ can be defined by introducing the porosity ε as [7,13]

$$\langle \varphi_f \rangle^f = \frac{\langle \varphi_f \rangle}{\varepsilon} \tag{3.6}$$

Another important definition is the spatial averaging theorem, which is defined as [7,13]

$$\langle \nabla \varphi \rangle = \nabla . \langle \varphi \rangle + \int_{A_{fs}} n \, \varphi \, da \tag{3.7}$$

where A_{fs} is the interfacial surface area of the REV within the averaging volume, and n is the unit vector normal to A_{fs}. Volume-averaging the products of properties is applied by decomposing a quantity into its intrinsic average and spatial deviation, and considering the volume-averaging of the spatial deviation insignificant. This concept will be explained in the following paragraphs.

The closure form of transport equations discussed later analyzes the pure fluid and solid constituents without the presence of inherent fuel. At first, the general mass conservation equation for the liquid or gas phases is [4,7,13,48]

$$\frac{\partial}{\partial t} \varepsilon \langle \rho_f \rangle^f + \nabla . \left(\langle \rho_f \rangle^f \langle u \rangle \right) = \langle \dot{m} \rangle_f \tag{3.8}$$

where $\langle \dot{m} \rangle$ represents the generation (source) or removal (sink) of mass per unit volume per unit time for the gas and liquid phases. Momentum equation can be derived as [7,13]

$$\frac{\partial \langle \rho_f \rangle^f \langle u \rangle}{\partial t} + \frac{1}{\varepsilon} \nabla . \left(\langle \rho_f \rangle^f \langle u \rangle \langle u \rangle \right)$$

$$= -\varepsilon \nabla \langle P \rangle^f + \mu \nabla^2 \langle u \rangle + \varepsilon \langle \rho_f \rangle^f f - \varepsilon \frac{\mu}{K} \langle u \rangle \tag{3.9}$$

$$- \varepsilon \frac{\langle \rho_f \rangle^f c_E}{\sqrt{K}} \langle u \rangle | \langle u \rangle |$$

The last two terms on the right-hand side of Eq. 3.9 (momentum) are the Darcy and Forchheimer terms, respectively, that represent the viscous and form drag resulting from the interaction between the solid and fluid-constituents in the porous media. Darcy term is a result of the microscopic viscous shear stresses applied by the porous matrix to the fluid. Forchheimer term is a representative of the microscopic inertial forces felt by the fluid as a result of form drag. In this sense, we need to find the closure coefficients K and c_E in the momentum equation. Theoretically, if the flow in the fluid-saturated porous domain takes place with low velocity and $Re = \rho v \frac{d}{\mu} < 1$, the modified Darcy flow model can be used, and the momentum equation reduces to [49],

$$v = -\frac{K}{\mu}(\nabla P - \rho g) \tag{3.10}$$

where v is the fluid phase velocity vector, d is the characteristic length, μ is the viscosity, K is the permeability, and g is the gravity vector. A gas equation that governs the relation between the thermo-physical properties of air within the domain is

$$\rho = \frac{P}{RT} \tag{3.11}$$

where ρ in the fluid density, P is the static pressure, R is the fluid constant and T is the fluid temperature. The macroscopic governing equations for the transport of momentum and energy in porous media are derived based on the volume averaging method indicated by Nield and Bejan [9] and Whitaker [13]. As a result, a representative elemental volume (REV) occupied by fluid and porous matrix is considered to generate the closure forms. Figure 3.2 represents an elementary volume.
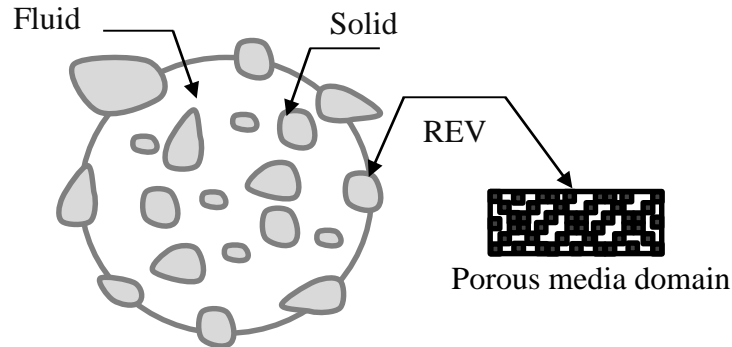
Figure 3.2: Schematic diagram of a representative elemental volume (REV).

3.2.2 Energy equations

3.2.2.1 Solid energy equation

For the solid energy, we start with two terms, the unsteady and the conduction.

$$\rho_s C_{p,s} \frac{\partial T_s}{\partial t} = \nabla \cdot (k_s \nabla T_s) \tag{3.12}$$

By applying the volume average in the first term

$$\left\langle \frac{\partial T_s}{\partial t} \right\rangle = \frac{V_s}{V} \frac{\partial}{\partial t} \frac{1}{V_s} \int_{V_s} T_s dV = (1 - \varepsilon) \frac{\partial \langle T_s \rangle^s}{\partial t} \tag{3.13}$$

and for the conduction term [13],

$$\langle \nabla \cdot k_s \nabla T_s \rangle = \nabla \cdot \langle k_s \nabla T_s \rangle + \frac{1}{V} \int_{A_{fs}} n_{sf} \cdot k_s \nabla T_s dA$$

$$= \nabla \cdot k_s \langle \nabla T_s \rangle + \underbrace{\frac{1}{V} \int_{A_{fs}} n_{sf} \cdot k_s \nabla T_s dA}_{interfacial\ heat\ flux} \tag{3.14}$$

and [13]:

$$\nabla \cdot k_s \langle \nabla T_s \rangle = \nabla \cdot \left(k_s \nabla \left((1 - \varepsilon) \langle T_s \rangle^s \right) + k_s \frac{1}{V} \overbrace{\int_{A_{fs}} n_{sf} \cdot T_s dA}^{Tortuosity} \right) \tag{3.15}$$

Note that the last term in Eq. 3.14 represents the interfacial heat transfer h_{sf}; in this sense, it is gainful to close this term by using Newton heuristic cooling law [13].

$$\frac{1}{V} \int_{A_{fs}} n_{sf} \cdot k_s \nabla T_s dA = -h_{fs} a_{fs} \left(\langle T_s \rangle^s - \langle T_f \rangle^f \right) \tag{3.16}$$

a_{fs} is the specific interfacial surface area and equal to $6(1 - \varepsilon)/d_p$. d_p is the particle diameter [4]. In order to close the tortuosity term, we employ the spatial average-deviation decomposition for simplification.

$$\frac{1}{V}\int_{A_{fs}} n_{sf} \cdot T_s dA = \langle T_s \rangle^s \frac{1}{V}\int_{A_{fs}} n_{sf} \cdot dA + \frac{1}{V}\int_{A_{fs}} n_{sf} \cdot \tilde{T}_s dA \tag{3.17}$$

$$\frac{1}{V}\int_{A_{fs}} n_{sf} \cdot T_s dA = -\nabla\varepsilon\langle T_s \rangle^s + \frac{1}{V}\int_{A_{fs}} n_{sf} \cdot \tilde{T}_s dA \tag{3.18}$$

By neglecting the porosity variation, we arrive at

$$\frac{1}{V}\int_{A_{fs}} n_{sf} \cdot T_s \, dA = \frac{1}{V}\int_{A_{fs}} n_{sf} \cdot \tilde{T}_s \, dA \tag{3.19}$$

so the updated version of Eq. 3.14 is

$$\langle \nabla. k_s \nabla T_s \rangle = \nabla.\left((1-\varepsilon)k_s \nabla \langle T_s \rangle^s + k_s \frac{1}{V}\int_{A_{fs}} n_{sf} \cdot \tilde{T}_s dA \right) \\ - h_{fs}a_{fs}\left(\langle T_s \rangle^s - \langle T_f \rangle^f \right) \tag{3.20}$$

In order to close the solid energy equation, the form adopted by Whitaker [13] and Kaviany [4] is

$$\tilde{T}_s = b_s \nabla \langle T_s \rangle^s \tag{3.21}$$

$\tilde{T}_s$ is the temperature deviation and b_s is a constant. This leads to the following expression,

$$\langle \nabla. k_s \nabla T_s \rangle = \nabla.\left((1-\varepsilon)k_s \nabla \langle T_s \rangle^s + \frac{k_s}{V}\int_{A_{fs}} n_{sf} b_s \cdot \nabla \langle T_s \rangle^s dA \right) \\ - h_{fs}a_{fs}\left(\langle T_s \rangle^s - \langle T_f \rangle^f \right) \tag{3.22}$$

Finally,

$$\langle \nabla. k_s \nabla T_s \rangle = \nabla. \left((1 - \varepsilon)k_s I + \overbrace{\frac{k_s}{V} \int_{A_{fs}} n_{sf} b_s . dA}^{k_{se}} \right) \nabla \langle T_s \rangle^s$$

$$- h_{fs} a_{fs} \left(\langle T_s \rangle^s - \langle T_f \rangle^f \right) \qquad (3.23)$$

As shown in the previous equation, a new term called solid effective conductivity lumps two terms. At this point, the solid energy equation has the full closure form [4,7,13].

$$(1 - \varepsilon)\rho_s C_{p,s} \frac{\partial \langle T_s \rangle^s}{\partial t} = \nabla. k_{se} \nabla \langle T_s \rangle^s - h_{fs} a_{fs} \left(\langle T_s \rangle^s - \langle T_f \rangle^f \right) \qquad (3.24)$$

3.2.2.2   Fluid energy equation

For the fluid equation, the unsteady, advection and the conduction terms are

$$\rho_f C_{p,f} \left[\frac{\partial T_f}{\partial t} + \nabla. (u T_f) \right] = \nabla. k_f \nabla T_f \qquad (3.25)$$

starting with the unsteady term,

$$\langle \frac{\partial T_f}{\partial t} \rangle = \frac{V_f}{V} \frac{\partial}{\partial t} \frac{1}{V_f} \int_{V_f} T_f dV = \varepsilon \frac{\partial \langle T_f \rangle^f}{\partial t} \qquad (3.26)$$

and the advection term is

$$\langle \nabla. (u T_f) \rangle = \nabla. \langle u T_f \rangle + \frac{1}{V} \int_{A_{fs}} n_{fs} . u T_f dA \qquad (3.27)$$

By applying the no-slip condition, the second term on the right hand side of Eq. 3.27 vanishes, thus

$$\langle \nabla. (u T_f) \rangle = \nabla \langle u T_f \rangle \qquad (3.28)$$

In order to decompose the velocity and temperature properties, spatial and deviation terms are presented as

$$u = \langle u \rangle^f + \tilde{u}_f \qquad (3.29)$$

$$T_f = \langle T_f \rangle^f + \tilde{T}_f \tag{3.30}$$

and after some assumptions and simplifications, Eq. 3.28 becomes

$$\langle \nabla . (\mathbf{u} T_f) \rangle = \nabla . \langle \langle u \rangle^f \langle T_f \rangle^f + \tilde{u} \langle T_f \rangle^f + \tilde{T}_f \langle u \rangle^f + \tilde{u} \tilde{T}_f \rangle \tag{3.31}$$

and

$$\langle \nabla . (\mathbf{u} T_f) \rangle = \nabla . \left(\varepsilon \langle u \rangle^f \langle T_f \rangle^f + \langle \tilde{u} \rangle \langle T_f \rangle^f + \langle \tilde{T}_f \rangle \langle u \rangle^f + \langle \tilde{u} \tilde{T}_f \rangle \right) \tag{3.32}$$

Note that the volume average of spatial deviation is zero

$$\langle \nabla . (\mathbf{u} T_f) \rangle = \nabla . (\langle u \rangle \langle T_f \rangle^f) + \nabla . \langle \tilde{u}_f \tilde{T}_f \rangle \tag{3.33}$$

By applying the Whitaker closure form [13]

$$\tilde{T}_f = b_f \nabla \langle T_f \rangle^f \tag{3.34}$$

and substituting in Eq. 3.33

$$\langle \nabla . (\mathbf{u} T_f) \rangle = \nabla . (\langle u \rangle \langle T_f \rangle^f) + \nabla . \langle \tilde{u} \, b_f . \nabla \langle T_f \rangle^f \rangle \tag{3.35}$$

$$\langle \nabla . (\mathbf{u} T_f) \rangle = \nabla . (\langle u \rangle \langle T_f \rangle^f) + \nabla . \left(\langle \tilde{u} \, b_f \rangle . \nabla \langle T_f \rangle^f \right) \tag{3.36}$$

For the conduction term, the procedure is similar to that of solid energy equation and leads to the following expression [13]

$$\langle \nabla . k_f \nabla T_f \rangle = \nabla . \left(\varepsilon k_f I + \frac{k_f}{V} \int\limits_{A_{fs}} n_{fs} b_f \, . \, dA \right) . \nabla \langle T_f \rangle^f$$
$$+ h_{fs} a_{fs} \left(\langle T_s \rangle^s - \langle T_f \rangle^f \right) \tag{3.37}$$

as a result, the extrinsic fluid energy equation is

$$\rho_f C_{p,f} \left[\varepsilon \frac{\partial \langle T_f \rangle^f}{\partial t} + \nabla. (\langle u \rangle \langle T_f \rangle^f) \right]$$

$$= \nabla. \left(\varepsilon k_f I + \overbrace{\frac{k_f}{V} \int_{A_{fs}} n_{fs} b_f . dA}^{Tortuosity} \right.$$

$$\left. \overbrace{- \rho_f C_{p,f} \langle \tilde{u}_f b_f \rangle}^{Dispersion} \right). \nabla \langle T_f \rangle^f + h_{fs} a_{fs} (\langle T_s \rangle^s - \langle T_f \rangle^f)$$

(3.38)

Similar to the solid energy equation and using fluid effective conductivity, the final closed form will be as [4,7,13]

$$\rho_f C_{p,f} \left[\varepsilon \frac{\partial \langle T_f \rangle^f}{\partial t} + \nabla. (\langle u \rangle \langle T_f \rangle^f) \right]$$

$$= \nabla. k_{fe} \nabla \langle T_f \rangle^f + h_{fs} a_{fs} (\langle T_s \rangle^s - \langle T_f \rangle^f)$$

(3.39)

3.3 Summary

As described earlier, the closure of the volume-averaged non-equilibrium transport equations requires the determination of the interfacial heat transfer h_{fs}, and the permeability K. For the sake of the solution, different methods could be applied at different scales to construct a geometric model at the microscopic scale level for the corresponding physics with the appropriate assumptions. At this point, the focus of this work is to identify a simple pore-level model that establishes the closure forms for the porous continuum associated with low computational time and cost. In the next chapter, a complete parametric study for three suggested methods including heat transfer and hydrodynamics comparisons portrays the thesis work.

Chapter 4

4   Microscopic CFD Analysis

This chapter will show a brief introduction about computational fluid dynamics (CFD) followed by a parametric comparison between a geometric model mathematically produced and a digitized image of a packed bed of sand. ANSYS and YADE [50] softwares are the CFD and geometric modelling tools respectively. Afterwards, the analysis will extend further to validate the CFD approach. In this sense, another study that compares experimental results of column of sand and those of a representative element volume (REV) based on YADE will be presented. A correlation for the sand and air relation will be developed at the end of the analysis.

4.1   Transport equations closure using CFD approach

The macroscopic (porous-continuum) model derived in the previous chapter showed that terms arising due to volume-averaging of the porous region require closure to complete the model. To this end, mathematical models have been introduced for the terms in question, but coefficients are required to be established to characterize a particular porous material. The coefficients are derived herein from thermofluid simulations of pore-level flow in a geometric representation of a REV. REVs of different geometric parameters (porosity, pore diameter) are simulated under isothermal particle conditions to establish the coefficients.

The choice to conduct these simulations under the isothermal solid condition was made on the basis of considering the relative resistances between the inside of the solid and the solid-fluid interface. If the Biot number, which represents the ratio of the conductive to convective resistance, is much less than one, the assumption of a uniform temperature distribution within the solid is reasonable [30]; i.e.:

$$Bi \equiv \frac{R_{cond}}{R_{conv}} = \frac{d/k}{1/h} \tag{4.1}$$

where R_{cond} is the conductive resistance inside the solid, R_{conv} is the convection resistance at the solid-fluid interface, d is the particle diameter, k is the thermal conductivity, and h is

the convective heat transfer coefficient. Since for the cases of interest in this work, *Bi* is much less than one, we can assume that the solid takes a uniform temperature such that no transport equations need to be solved in the solid region.

Closure for each of the constitutive relations appearing in the momentum and energy equations needs special treatment. The data required for closure is obtained from pore-level computations on a suggested REV based on some analysis (described later); that characterizes a packed bed of particles and will be discussed in detail in subsequent sections. Closure of the Darcy and Forchheimer drag terms appearing in Eq. 3.9 is achieved by considering the pore-level hydrodynamics of the REV. The predicted pressure drop across the REV is utilized to evaluate the permeability K and inertial coefficient c_E as

$$\frac{\Delta P}{L} = -\frac{\mu}{K}\langle v \rangle - \frac{\langle \rho_f \rangle^f c_E}{\sqrt{K}}\langle v \rangle |\langle v \rangle|$$

(4.2)

where, ΔP is the pressure drop across the length L of the REV. The first and second terms were introduced in the previous chapter. The first term on the right side is the Darcy term and the second one is the Forchheimer term (form drag). In this work, we neglect the second term since the studied flow has a very low velocity. As a result, for each geometric model, linear behaviour in the low Re_d region may be assumed to calculate K. Since the REVs generated from YADE are spatially periodic in all principle directions (described more in next section), three complete calculations are done on each REV; one for an imposed flow in the x-direction, one for an imposed flow in the y-direction, and one for an imposed flow in the z-direction. In this manner, three sets of low results are available for each REV produced. The pressure drop is calculated for each flow direction and then averaged as follows [30,39]:

$$\frac{\Delta P}{\Delta x} = -\frac{1}{3}\sum_{x,y,z}\frac{P_{in} - P_{out}}{x_{in} - x_{out}}$$

(4.3)

The closure of the macroscopic, non-equilibrium heat transfer equation requires determination of the interfacial heat transfer coefficients h_{fs} along with the effective thermal conductivity k_{eff}. Under fully developed conditions and constant surface

temperature, and neglecting the heat transfer by conduction in the axial direction, the interstitial convection coefficient is established by considering convective heating of a fluid through an isothermal domain. As with the calculation of pressure drop, results for heating are obtained from three sets of computations on the same domain and then averaged to obtain the final coefficient for a given REV [30]:

$$h_{fs} = -\frac{1}{3}\sum_{x,y,z}\frac{\dot{m}c_P}{A_{fs}}\ln\left(\frac{T_p - T_{out}}{T_p - T_{in}}\right) \tag{4.4}$$

where, A_{fs} is the interfacial surface area of the REV, $\dot{m}$ is the mass flow rate through the REV, c_P is the specific heat capacity, T_p is the constant isothermal particle surface temperature of the solid-constituent, T_{in}, T_{out}, P_{in} and P_{out} are the mass flow-averaged bulk fluid temperatures and pressures at the inlet and outlet of the REV, respectively.

For k_{eff}, as explained in Chapter 3, we start from:

$$k_{eff} = k_{cond} + k_{disp} + k_{tor} \tag{4.5}$$

where k_{disp} is defined in Eq. 3.38 as:

$$k_{disp}.\nabla\langle T_f\rangle^f = -C_{p,f}\langle\rho_f\rangle^f\langle\varepsilon\tilde{u}_f\tilde{T}_f\rangle^f \tag{4.6}$$

and after further simplifications

$$k_{disp} = -\varepsilon\frac{C_{p,f}\langle\rho_f\rangle^f}{\nabla\langle T_f\rangle^f}\left(\langle u\rangle - \langle u_f\rangle^f\right)\left(\langle T\rangle - \langle T_f\rangle^f\right) \tag{4.7}$$

It is useful to mention herein that although the dispersion effect can be easily modelled using Eq. 4.7, it can be neglected in the present work as Reynolds number is extremely small. In addition, the tortuosity term is neglected due to the isothermal assumption of the solid constituent of porous media.

In the pore-level CFD simulations, the mass flow rate along the flow direction was imposed according to the flow Reynolds number. The inlet and outlet faces are to be those perpendicular to the flow direction and the mass flow rate is evaluated as [4,35]

$$\dot{m} = L^2 \rho_f U \tag{4.8}$$

where the side length L of the REV is obtained from YADE following geometry generation and the extrinsic flow velocity U is calculated from the Reynolds number, which is defined as

$$Re_d = \frac{Ud}{\nu} \tag{4.9}$$

Periodic boundary conditions are enforced on all other pairs of faces.

4.2 Fundamentals of geometric modelling (CFD-YADE)

Applying a geometric modelling of an entire packed bed of spheres is not reasonable. That is why utilizing REVs with random arrangements of particles can characterize a small portion of a much larger packed bed. The approach adopts the formulation developed by Dyck and Straatman [21], except using a modified contact law [51] that was developed for spherical particles. Their approach produces three-dimensional domains of randomly packed spheres using YADE, with spatial periodicity maintained in the x, y and z directions. CAD models of the REVs are created using Solidworks™ [52] and then meshed by ANSYS Meshing™ tool [53]. (See Fig. 4.1)

The computational time needed to generate the REV is slightly different. For small number of spheres, it may take few to tens of minutes to finalize. On the contrary, as the number of particles reaches hundreds, a few hours may be needed. This time is considered low if we compare with other techniques such as scanning the studied shape or analyzing the same shape in experimental laboratories.
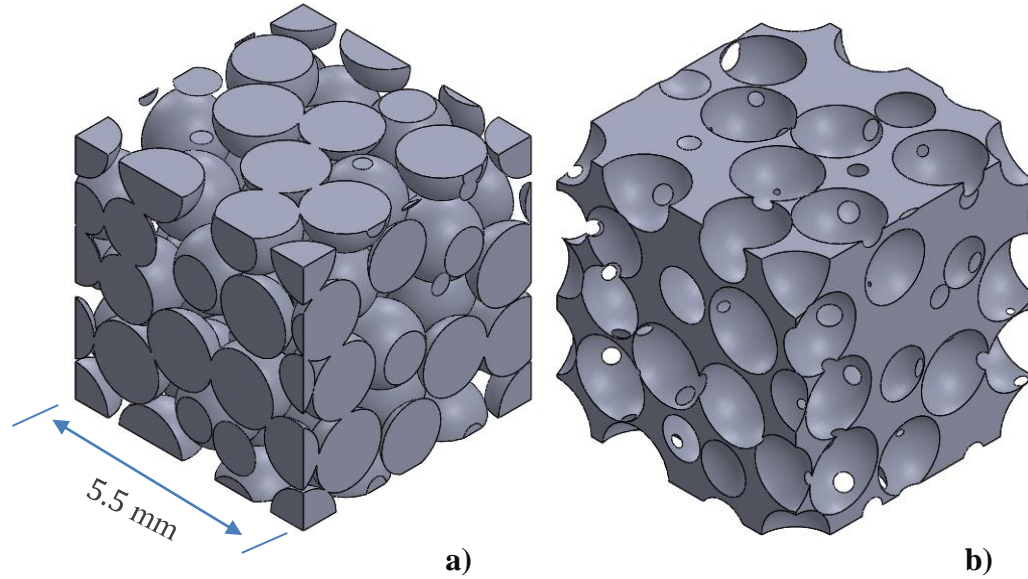
Figure 4.1: (a) Proposed REV of a packed bed of particles (spheres), and (b) Geometric idealization representing fluid region. (50 particles, d=1.59 x 10^{-3} m, and ε=0.37)

The way to generate a particular REV is to estimate the quantity of particles inside the REV along with their diameter (equivalent length), and the target porosity. The model places the spheres (primitives) inside of a three-dimensional box and then compresses the box allowing the spheres to collide and shift based on the contact law [51] until the final porosity is achieved. In order to avoid generating poor quality meshes at contact points between particles, slight deformation was allowed to generate better topology of meshing surface as shown in Fig. 4.1(b). Point contacts between particles may cause separation in mesh elements. In the following analysis, the physical properties for the upcoming case is shown in Table 4.1 also, the allowed diameter deviation is $d\pm\in\{0.05, 0.1, 0.2\}d$, meaning that $\{10\%, 20\%, 40\%\}$ of total deviations of the mean diameter are allowed in this case.

Table 4.1: Physical properties of the studied case.

Particle Diameter	Porosity	Re	Pr	T_p(Particle Temperature)	T_{in}(Inlet Temperature)
1.59 x 10^{-3} m	0.37	6.5	0.7	250 °C	25 °C

Fig. 4.1(b) shows the portion of a proposed REV that requires discretization for the CFD simulation. The fluid (void) space in the REV was discretized using the ANSYS Meshing™

tool [53] and pore-level simulations of the REVs were carried out using the commercial CFD software ANSYS® CFX™ [54]. Since the meshing size of the REV varies with the porosity and sphere diameter, the criteria of grid independence of the domain was based on the ratio of mean sphere diameter (*d*) to the meshing element size. Table 4.2 shows the grid independence.

Table 4.2: Grid independence of normalized properties for the studied case.

Cell number (million)	Particle Diameter(m)	Element size(m)	d/mesh element	$\Delta P/L$ (Pa/m)	Nu
0.5	1.59 x 10^{-3}	1.40 x 10^{-4}	11.357	803.586	3.679
1	1.59 x 10^{-3}	8.00 x 10^{-5}	19.875	947.541	3.554
2	1.59 x 10^{-3}	5.50 x 10^{-5}	28.909	1038.567	3.476
4	1.59 x 10^{-3}	4.20 x 10^{-5}	37.857	1110.434	3.429

The analysis of grid independency is achieved to within 6% and 1.1% for the normalized pressure and Nusselt number (Nu) respectively when the ratio reaches approximately 38, which reflects mesh size of the order of four million cells.

Heat transfer and hydrodynamics were incorporated by solving the energy transport equation; momentum and mass equations among the pore-level constituents. In general, the advection scheme QUICK was utilized for all the transport equations, and pressure–velocity coupling was achieved by employing the SIMPLEC algorithm. The convergence of the simulations was enhanced by slightly modifying the default under-relaxation factors given in case of Fluent™ [55]. High resolution advecting scheme was applied in the case of ANSYS® CFX™ [54]. The incompressible ideal gas model was selected with air as the working fluid in this study. The steady-state problem was simulated until the scaled residuals of all the transport equations converged to the root mean square below 10^{-4}. Both software could mimic the same model with almost the same computational time and output results.

No-slip hydrodynamic conditions were imposed at the isothermal surfaces of the spheres for all the simulations (see Solver Theory Guide for the details of boundary condition implementation either for Fluent™ [56] or CFX™ [57]). The transient problem of cooling

could be simplified to a steady-state based on the fact that in the fully-developed region, the Nusselt number does not change in time.

4.2.1   Minimum number of particles

In order to perform the heat transfer and hydrodynamics analysis, it is preferable to determine the minimum number of particles inside a proposed REV so that the closure coefficients for transport equations do not change significantly beyond this limit. Figure 4.2 shows the results of the dimensionless Nusselt number assuming no diameter deviation. The selected number of particles (spheres) $\in \{25, 50, 100\}$ were tested considering Nu as a comparison of this analysis. Nevertheless, Fig. 4.3 depicts the outputs based on the same cases of REVs but with different ranges of particle deviation. The diameter deviation is allowed to vary as $d \pm \{0, 5\%, 10\%\}d$ with total variation of $(0, 10\%, 20\%)$ of the mean diameter. The suggested mean diameter for this analysis was considered as 1.59 x 10^{-3} m.

It is obvious that near 50 particles, all cases' results collapse almost to the same points. This mainly refers to the interstitial area that characterizes the heat transfer behaviour inside the REV. In fact, allowing the variation of particles' number can slightly alter the final results when the number is higher than 50. The reason behind that is the functionality
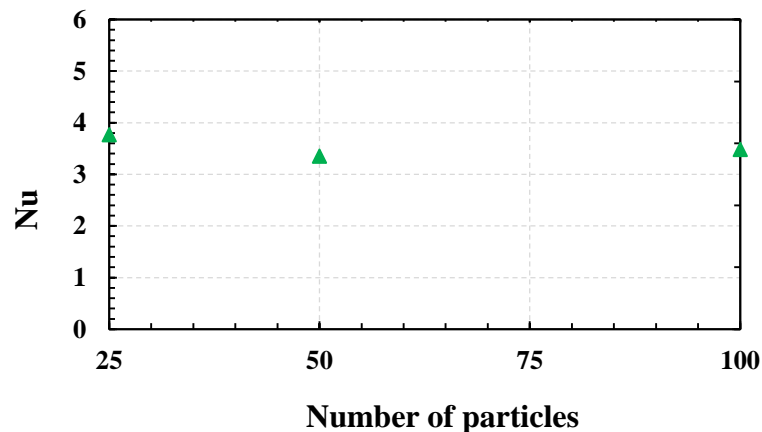
Figure 4.2: Nusselt number versus different number of particles at fixed diameter.

of YADE software in generating the REVs as explained earlier. However, two cases out of three kept the same results. It was found that at least 50 spheres are required to ensure that the CFD results are independent of the REV size.
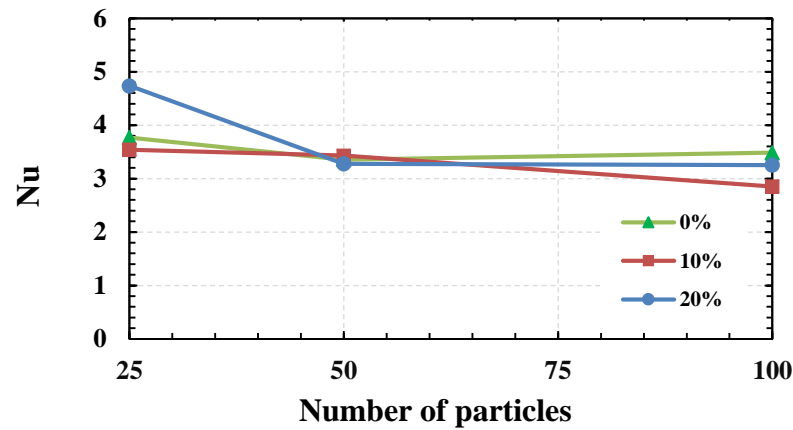
Figure 4.3: Nusselt number versus different number of particles at different diameter deviations.

4.2.2   Sphere diameter deviation

As the closure of energy equation is sought, Nu is considered to be our main dimensionless number for parametric analysis in this work. The diameter deviation is allowed to vary as $d \pm \{0.5\%, 10\%, 20\%\}d$ with total variation of $(0,10\%,20\%,40\%)$ of the mean diameter (1.59 x 10^{-3} m and 50 particles). Figure 4.4 shows that the total variation of particle diameter is not a function of Nu. This refers to the fact that interstitial surface area has no influence on the variation of sphere diameter since the surface area of bigger spheres compensates the smaller ones. As a result, the total surface area with respect to the REV volume is conserved for specific particle diameter. However, the number of spheres in addition to the selection method of certain diameter may add another factor to the previous conclusion. The length of the studied REV measured 5.5 mm as in Fig. 4.1.
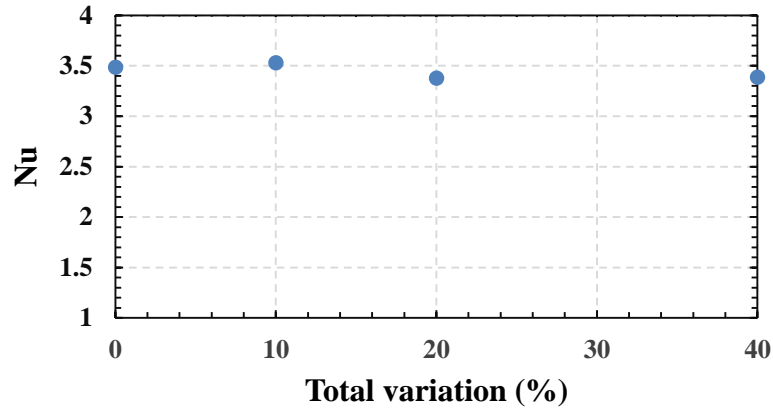
Figure 4.4: Nusselt number as a function of total variation of particle diameter

4.3 Segmented image of sand

As previously mentioned, one of the main goals of this study is to seek a closure model for a randomly packed bed of sand. A CFD approach was first applied to realize this target, where a number of particles are compacted such that the new cell is defined a REV. The applicability to simulate the fluid flow in a dimensionally defined REV, is often of high interest. That is why for this research an additional comparison between the results of scanned image of sand particles and YADE REV approach will help to identify the credibility and viability of the REVs generated by YADE software. (The raw file of the digitized image including its data sets was obtained from Ian Molnar).

In the segmented image approach, a set of selected images are mainly scanned by applying a specific imaging procedure required for SXCMT (Synchrotron X-ray Computed Microtomography) technique of uniform quartz in a porous medium [58,59]. Moreover, it is about a 3D dataset of X-ray image averaged over a 9.87×9.87×9.87 μm for each direction, where the voxel resolution is 9.87 μm/voxel [19,58]. Each image needs roughly 40 minutes of imaging time in order to finalize the scan. The output is a REV of 350×350×450 voxels precisely cropped so that the final dimensions of the selected image is 3.45×3.45×4.44 mm as shown in Fig. 4.5(a) [19]. Figure 4.5(b) represents a mid-plane cross section of the scanned image and depicts the fluid region with red color around the sand [19].

4.3.1   Imaging, reconstruction and segmentation

Imaging was completed at the Argonne National Lab, Advanced Photon Source Synchrotron, 13-BM-D beamline with the GSECARS research group [19,58]. The imaging reconstruction procedure and equipment used are detailed in [19]. In this technique, collected projections were reconstructed into three-dimensional data sets using GSECARS specific reconstruction software [60].

The reconstruction software applied filtered back projection with a radon transform and special filter so that a three-dimensional map of X-ray linear mass attenuation values were obtained [19]. The images were checked to ensure that the segmentation properly identified the grain-fluid boundaries [19]. Table 4.3 presents the physical properties of the segmented image [19].

Table 4.3: Geometric properties for the digitized image [19].

Porous Media	Porosity	Sleeved Grain size (d)	Fluid
Uniform Quartz	33%	420-600 μ m	Air

4.3.2   Image post-processing

After scanning, cutting, and image acquisition were performed, the images were converted into a STL (Stereo-Lithography) file by ImageJ (An open platform for scientific image analysis) (http://imagej.net/) and an ImageJ plugin called BoneJ (Plugin for image analysis for ImageJ) (http://bonej.org/). ImageJ was applied for binarizing the gray-scale values of the images by filtering and thresholding processes. BoneJ was used to compute an iso-surface from the binarized images and write the STL file. The STL file contains a surface representation of the sand particles as shown in Fig. 4.5(a).
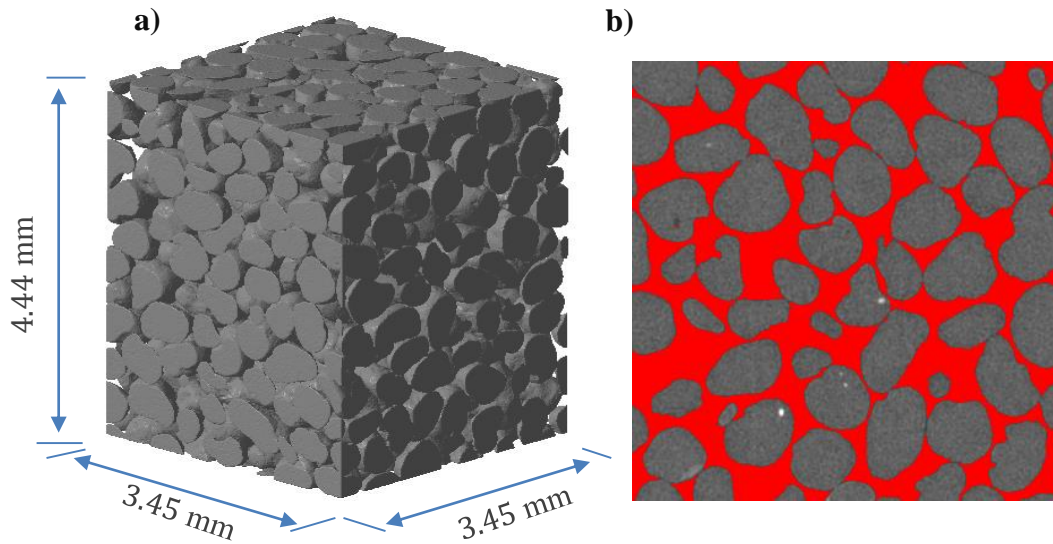
Figure 4.5: a) Scanned image of sand, and b) Mid-plane cut-out of the image [19].
Reproduced image.

A consistency check of the STL file was performed in MeshLab
(http://meshlab.sourceforge.net/), then the mesh surface of the sand particles was smoothed
and decimated. The geometry was created by importing the STL file into ANSYS-ICEM™
software [61]. The fluid continuum that surrounds the sand was achieved by subtracting
the sand volume from a cubic that surrounds the particles region. The idea of filling the
voids between the sand is vital herein. A primary model of the flow geometry is depicted
in Fig. 4.6 where the green color is the fluid.
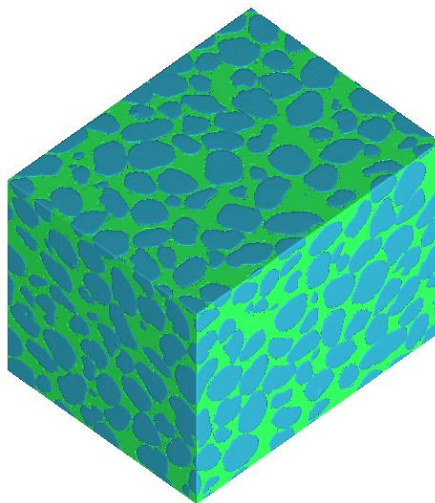
Figure 4.6: Image REV composed of sand and surrounded fluid (air).

The tetrahedral mesh was adopted to fill the fluid continuum. Refinement near the sand surface secured the quality of continuous mesh. The mesh size was composed of approximately between 4-6 million cells. Due to recirculation zones and tortuous paths, an extended region on each dimension applied a solution that overcomes the divergence issues and ensures steady state at the exit. Figure 4.7(a) presents the adjusted mesh in the flow direction. A cross-section of the geometry parallel to the flow is depicted in Fig. 4.7(b). Simulations applied in x, y and z directions result in average values for all studied quantities.

4.3.3   Building a REV counterpart to digitized image

To construct a representative element volume with the same porosity and particle diameter similar to the scanned image, the volume fraction of solid phase that determines the number of sand particles based on the data of Table 4.3 should be applied

$$\frac{V_s}{V} = 1 - \varepsilon = 1 - \frac{V_f}{V} \tag{4.10}$$
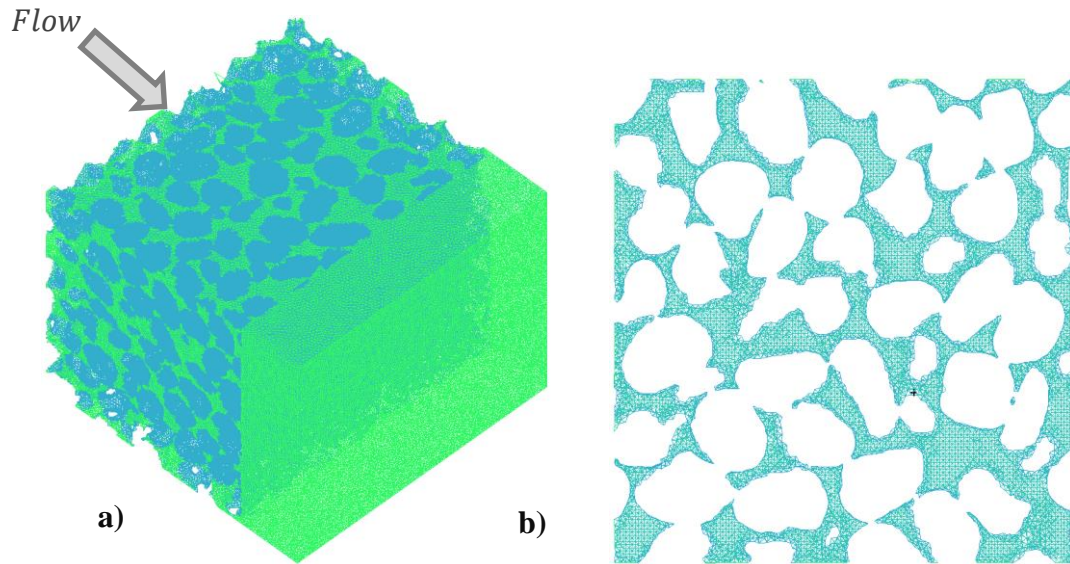
Figure 4.7: (a) 3D mesh of digitized image adjusted by adding extra length at the image exit, and (b) Cut-out at the mid-plane parallel to the flow without the extended length.

where ε is the porosity, V_f is the fluid volume and V is the volume of both constituents of the REV.

Fluid and solid particulate phases can be modeled by Eulerian-Eulerian approach. It is a common method that describes the motion of fluid and particles from a continuum point of view. As YADE [50] produces random packing of spheres inside the REV in all three directions, each REV is slightly different in terms of its geometry. As a result, there is no preferred direction to study the flow; thus each REV produced was used to simulate three cases of flow hydrodynamics and heat transfer in the x, y and z directions. The results of the average of three simulations lead to mean values for all quantities. Figure 4.8 shows a REV model composed of solid and ghost (near the surfaces) particles.
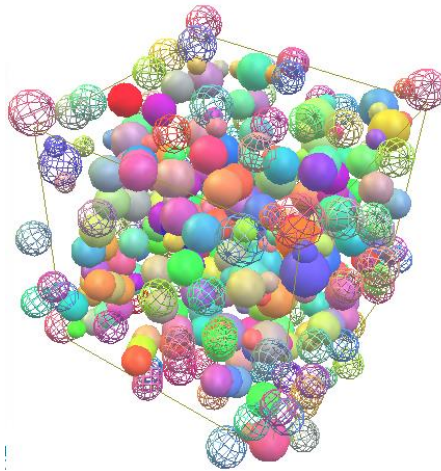
Figure 4.8: YADE model is comprised of particles (spheres) bounded by cubic lines. Ghost spheres represent periodic effect.

Back to Table 4.3 and after simple manipulations, the particles number that simulates the same geometry as the digitized image was around (512) based on the mean diameter assumed (510 μm) of spherical particle of sand. Figure 4.9 presents the final geometry of the generated REV produced in Solidworks™ [52]. Periodic boundary conditions were imposed on all pairs of parallel faces of the REV. The mass flow rate along the flow direction was used to impose a flow Reynolds number in the inlet face. An outflow boundary condition was enforced at the exit face. The temperature difference between the particles surface and the inlet face is 25°C and only the void phase which represents the

fluid part of the cube was discretized. By this way, we only needed to simulate the fluid zone, neglecting the solid part. This technique is accepted due to the isothermal assumption of the particles. The significant reduction of mesh elements reduces the computational time. The counterpart REV measures 3.78 mm in x, y and z directions, and the REV is periodic in all parallel faces.
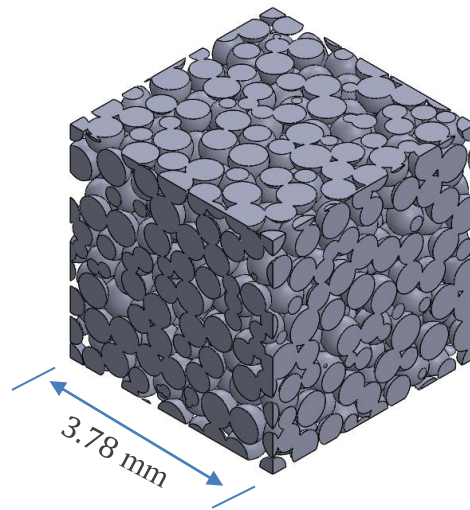
Figure 4.9: YADE REV of spherical particles with same geometric properties as digitized image.

As mentioned in the previous section, the generated mesh was elongated in the same direction of the flow. To do so, a growth rate between 1.2-3 was adopted so that the elements number of the added region is low. This technique was applied to reduce the computational time. See Fig. 4.10.
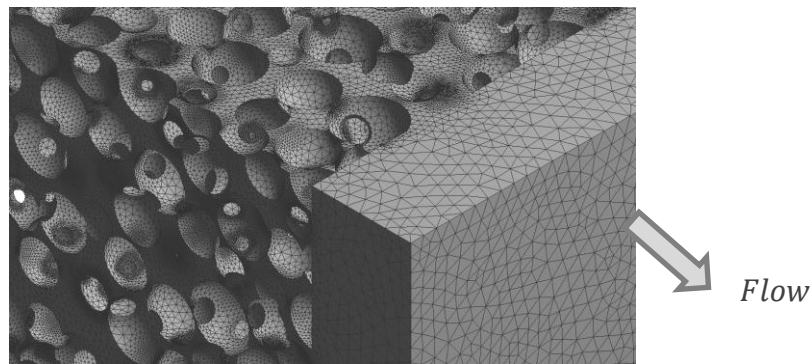
Figure 4.10: Mesh generated in ANSYS meshing™ Tool for the counterpart REV.

4.3.4   Results and discussion

In order to discuss the results, it is important to present the fluid flow occurring inside one of the previous geometries. Figure 4.11 depicts the velocity field inside the sand REV at Reynolds number of 10. It shows the flow spatial deviations of the velocity inside the packed sand. We could distinguish between high and low velocity zones. At the exit, with extension of 0.2 of the length, the reversed flow was lowered to 3-5%. If this region is removed, reversed flow at the exit may pass 20% decreasing the possibility of convergence. Steady state solution is critical since we seek the final state of heat transfer and hydrodynamics behaviour in the digitized image.

For the heat transfer, at the inlet of both shapes the characteristic length is observed within a short distance then, the flow becomes almost uniform. Figure 4.12 shows the image and YADE REVs heat transfer behaviour at the particle temperature of 523K. The region of flow progress is obvious and it only needed small distance until the shape of developed profile is achieved.
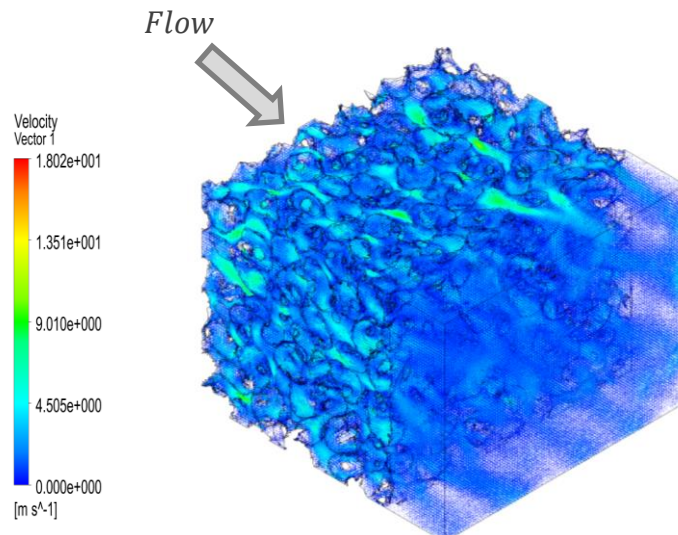
Figure 4.11: Velocity vector field of the digitized image at Re=10 and Pr=0.7. Extension length has been added to mitigate the reversed flow effect.
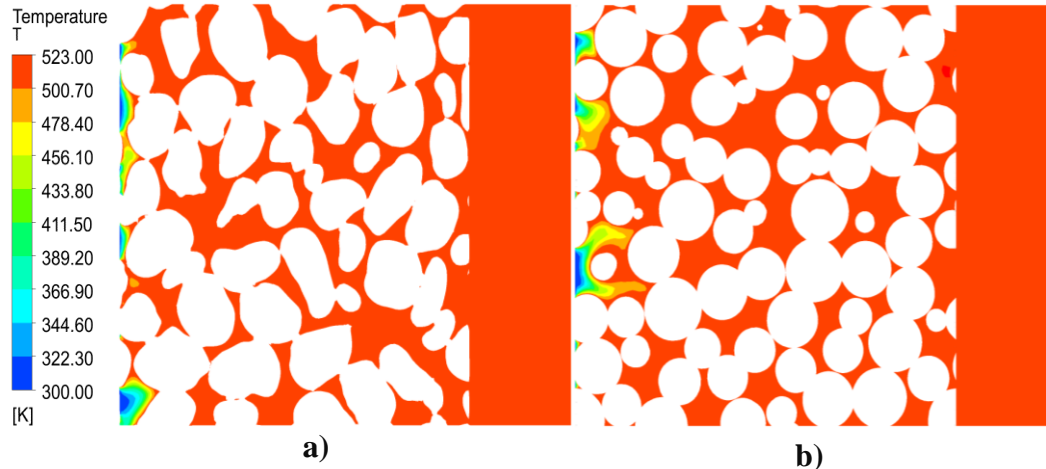
Figure 4.12: Mid-plane distribution of fluid temperature variations for (a) Digitized image, and (b) YADE REV. Re$_d$ =10 and Tp=523K.

Figure 4.13 and 4.14 shows the outputs for heat transfer and hydrodynamics of the studied cases for Re $\in \{1,2.5,5,7.5,10\}$. Concerning the results, the deviations of the heat transfer results were 23.19% at low Reynolds number and 3.44% at high value due to the increase of convective heat transfer effect. For the hydrodynamics behaviour, pressure drops of the image have approached those of the spherical shape due to the low Reynolds numbers applied herein. It acted in the same way and reached 5.9% at high Reynolds. Based on the previous analysis, it is clear that the YADE model yields the same trends as the digitized image. The cost of producing an image is extremely high compared to a YADE geometry with same properties. Moreover, the computational time dedicated to generate a YADE model is very short with respect to the scanned-image model. At pore-level scale and for different type of elements, YADE could produce different types of geometries with the same properties even with particles other than spheres (see Chapter 6).
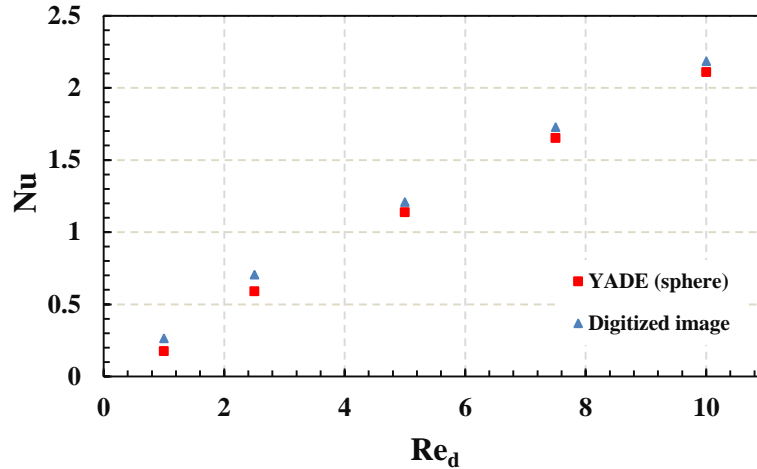
Figure 4.13: Comparison between REVs based on Nusselt number versus Reynolds number at the temperature difference of particles (T_p) and inlet flow (T_{in}) equal to 25°C, and Pr=0.7.
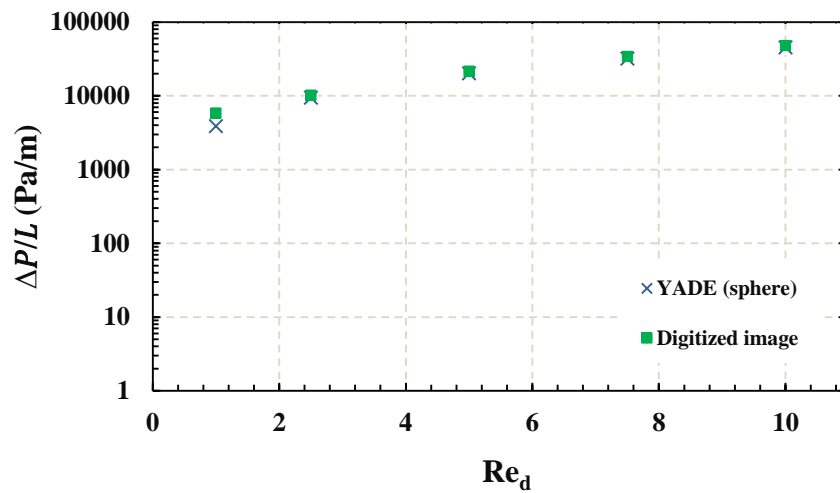
Figure 4.14: Comparison between REVs based on Pressure drops through the length (L) of the scanned image and YADE model.

4.4 Validation of YADE REV against experimental results

The outputs of the model presented in section 4.2 were compared with experimental results [20], with the focus on heat transfer. For the experimental work, measurements of temperature at different times are provided for a packed bed comprised of approximated

spherical particles. Measurements were obtained for a heat wave (pulse) propagating via convection through otherwise cold sand. The measurements are taken for the central packed channel to minimize the effect of the walls. These experiments – usually one-dimensional – were analyzed with numerical simulations based on an inverse computational technique. On this basis, estimates of the interfacial heat transfer coefficient were obtained. Constant and variable properties of air were applied in this technique [20]. In general, applying thermophysical properties as a function of temperature is more realistic (more detail about the experiment is presented in Chapter 5).

It is important to mention here that for Bi $\ll$ 1, the temperature gradients in the solid are small and the assumption of a uniform temperature distribution $T(x,t) \approx T(t)$ is reasonable [30]. In this study case, the previous limit of Biot number is violated when h_{fs} exceeds 210 W/m^2.K (see Chapter 5 for sand properties). In addition, due to the low value of Rayleigh number (Ra<<1), the buoyancy effect in forced convection may be disregarded [62] also, radiation is not considered at the microscopic scale level due to the fact of the isothermal analysis of solid constituent.

The plot given in Fig. 4.15 shows that the results derived from pore-level simulations on the YADE model are in reasonable accordance with the Wakao [40] model in terms of magnitude and trend. Note, however, that the results of the Wakao model in this region are extrapolated. Compared to the experimental results of [20], the present results give the same trend in terms of Re, but are considerably higher across the range of Re. The large differences could be due to the reverse approach used in [20] to obtain the results, which required an estimation of the heat loss from the test rig and an accurate estimate of the energy input over the heating period. It could also be partly attributed to the fact that computations were done herein for a heating condition, whereas the experimental results in [20] were derived from a combination of heating and cooling. Moreover, the difference could also be due to the fact that the YADE simulations did not account for the heat transfer to any proposed type of boundary conditions (heat loss) and, did not consider the variation of thermophysical properties of the solid constituent due to the isothermal assumption of the particle surface.
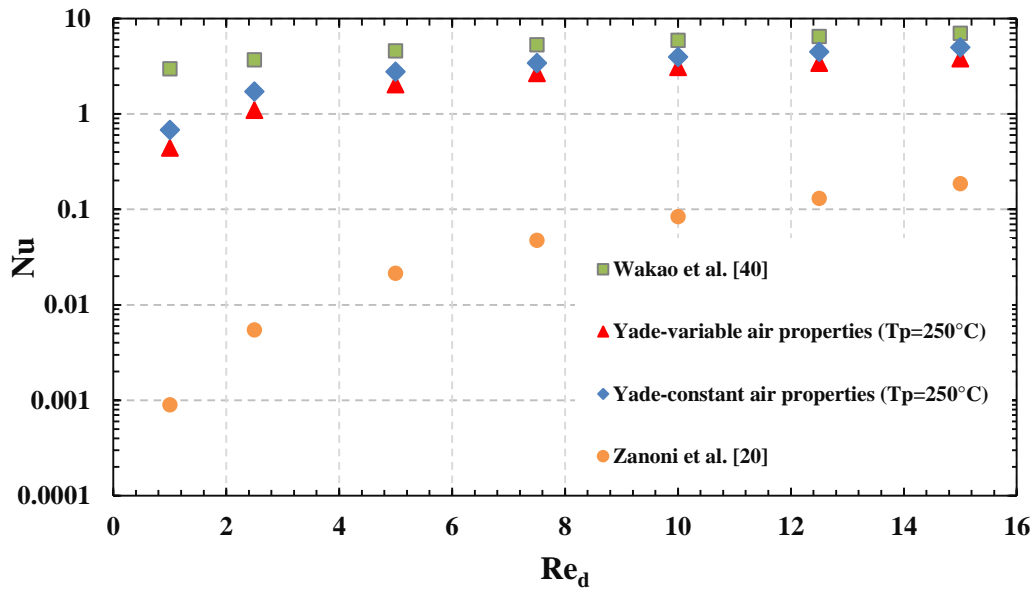
Figure 4.15: Comparison between numerous cases based on Nusselt number at different values of Reynolds number, and Pr =0.7.

The heat transfer coefficient h_{fs} is not a thermophysical property, but rather an interface property that is dependent on thermophysical properties like viscosity, conductivity, flow regime and geometry. If the temperature (bulk or surface) of the fluid varies in the flow direction, the value of the convective heat transfer coefficient (which depends on the temperature-dependent properties of the fluid) also varies in the flow direction. This effect is more highlighted in the high stream-wise temperature gradients on the surface. In this sense, h_{fs} can change substantially if fluid properties change. In other words, the heat transfer coefficient is dependent upon the fluid-to-wall temperature ratio [63].

A similar effect can be noticed by a subsonic flow in tubes at high surface and fluid temperatures. Figure 4.16 depicts the Nusselt number variation versus the ratio of surface to bulk temperature. The output lines have increasingly greater negative slopes as the temperature at which the fluid properties are evaluated, is increased.
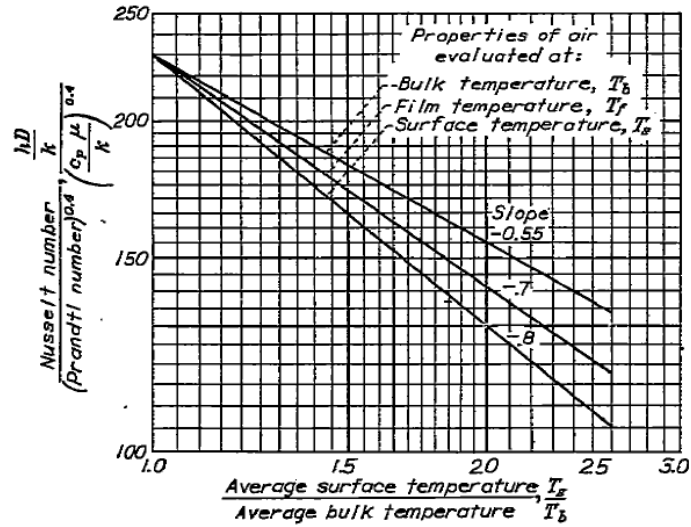
Figure 4.16: Variation of Nusselt number with the ratio of surface-to-bulk temperature using conventional methods of correlating heat transfer coefficients [64].

Additional analysis has been conducted to study the impact of solid temperature on the heat transfer between the particles and air. For this purpose, different flow cases of Reynolds number as Re $\in \{2.5, 5, 7.5, 10, 12.5, 15\}$ were simulated on the REV at $T_p \in \{323, 423, 523, 623, 723, 823, 923\}$ K. Due to solid surface temperatures increase, fluid physical properties were set to vary with respect to the local temperature. 6th degree polynomial functions were used for conduction, density, viscosity and specific heat of air derived as shown in Appendix (B) [30].

Figure 4.17 shows that accounting for the influence of temperature on air properties has a significant impact on the present results. In general, and according to the CFD results for each REV studied, volume-averaged of air properties were much closer to particle temperature.
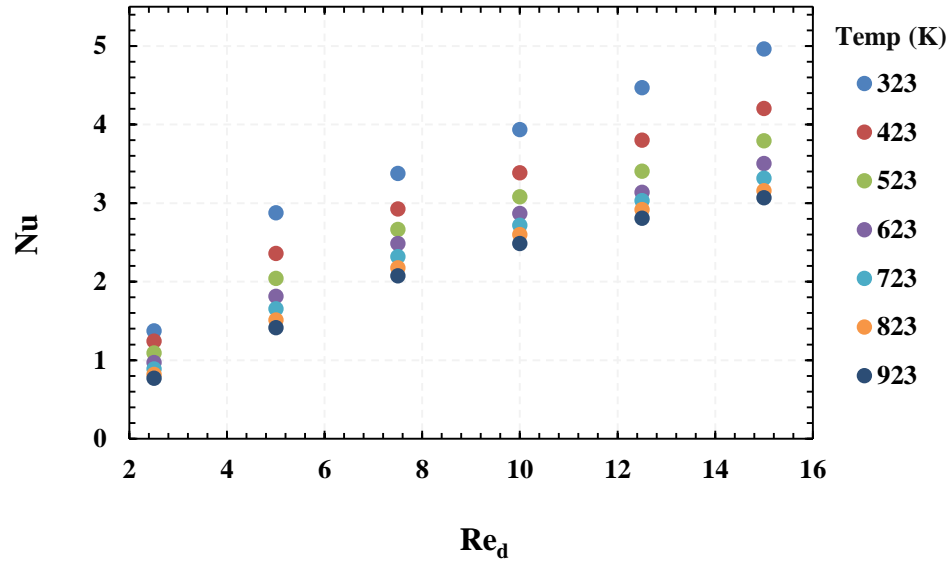
Figure 4.17: Nusselt number (averaged temperature) variation with respect to Reynolds number and solid temperature, and Pr=0.7.

Based on the previous Figs. (4.15-4.17), a correlation for the convective heat transfer coefficient is developed based on the present pore-level computations as a function of *Nu, Re* and *Pr*. Because detailed information on the thermofluid properties and the temperatures of the constituents are available from the present calculations, a correlation similar to Kalganova's [65] is adopted for the current study using the regression analysis package available in Matlab software for ease implementation into the volume-averaged framework. It takes the form of a power-law regression developed to provide a new empirical correlation for the heat transfer between sand and air as in Eq. 4.11.

$$Nu = a\frac{k_w}{k_\infty} + bPr_\infty^{1/3}Re_\infty^{0.5}\left(\frac{\rho_\infty\mu_\infty}{\rho_w\mu_w}\right)^c\left(\frac{c_{p\infty}}{c_{pw}}\right)^d \quad Pr = 0.7 \quad (4.11)$$

where the variables are as follows, Nu is the Nusselt number, k_w is the thermal conductivity of air at solid surface temperature, k_∞ is the thermal conductivity of bulk flow, μ_w is the viscosity of air at solid surface temperature, μ_∞ is the viscosity of the bulk flow, c_{pw} is the heat capacity of air at solid surface temperature , $c_{p\infty}$ is the heat capacity of the bulk flow, ρ_w is the density of air at solid surface temperature, ρ_∞ is density of bulk flow, and a, b, c and d are coefficients and , it was found that they have the values as shown in Table 4.4.

Table 4.4: Constant coefficient of Eq. 4.11. These coefficients were produced using variable thermodynamic properties of air.

a	-0.376
b	1.579
c	-2.077
d	-3.789

Figure 4.18 shows both simulated and correlated data at different temperature cases for the selected range of Reynolds number.
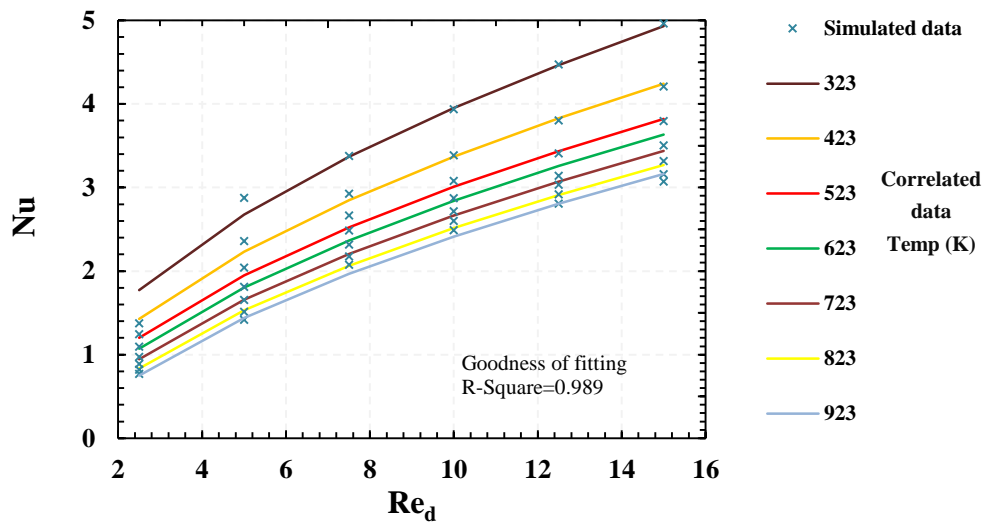
Figure 4.18: Comparison between the simulated and correlated data applying Eq.4.11. See Fig. 4.17 for more details about the simulated data.

Concerning the hydraulic behaviour, the permeability can be found from Darcy-Forchheimer equation (Eq. 4.2) and for creeping flow ($Re_d \approx 0.1$), it was found that the permeability for this case is 2.263 x 10^{-09} m^2. As presented earlier in chapter one, Karman-Kozeny model (Eq. 1.3):

$$K = \frac{\varepsilon^3 \, d^2}{a(1-\varepsilon)^2} \qquad (1.3)$$

which was initially developed for creeping flow in a packed bed of spherical particles is applied in order to be compared with the computational result. The permeability is calculated as 1.79 x 10^{-09} m^2, which is close to the one numerically calculated.

The variations of pressure drop $\Delta P/L$ with the Reynolds numbers and particle temperatures are shown in Fig. 4.19. It shows that as Reynolds increases, the pressure drops of different particle's temperature increase. In the region of low Reynolds numbers, the viscosity effects dominate thus, the hydrodynamics effect in the packed bed of spheres is quite low. However, since the tortuosities of random structures are much higher compared to a structured bed, the pressure drops would be greatly increased. The effect of temperature increase in the viscosity is clear. Thus, the ability of fluid movement decreases which increases the friction effect on the boundary layer within the same scale of REV.
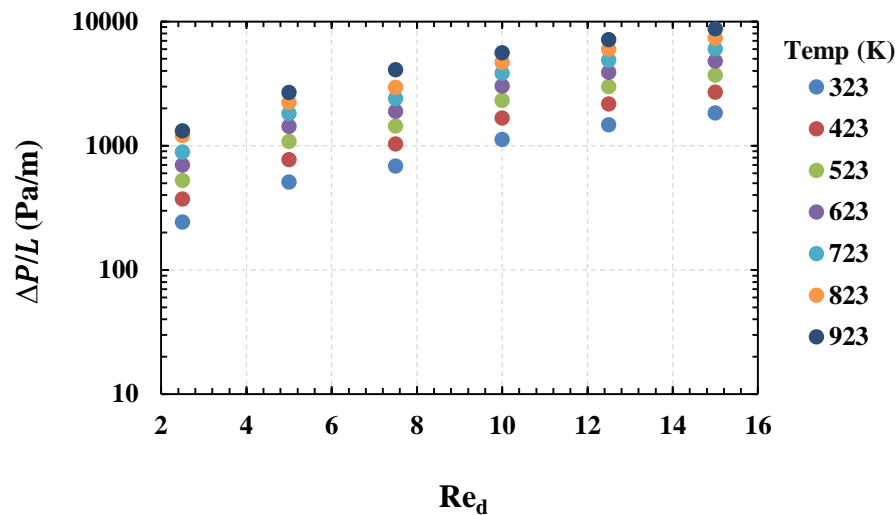
Figure 4.19: Pressure drop versus particles temperature at different Reynolds numbers.

The variations of Nusselt number explained earlier and the overall heat transfer efficiency (γ) of spheres to fluid is shown in Fig. 4.20. It shows that as the Reynolds number increases, the heat transfer performance is obtained at cost of high pressure drop. This cost can also be noticed at high temperatures. This figure is important in understanding the effect of bed type on the flow behaviour based on the selected porosity.
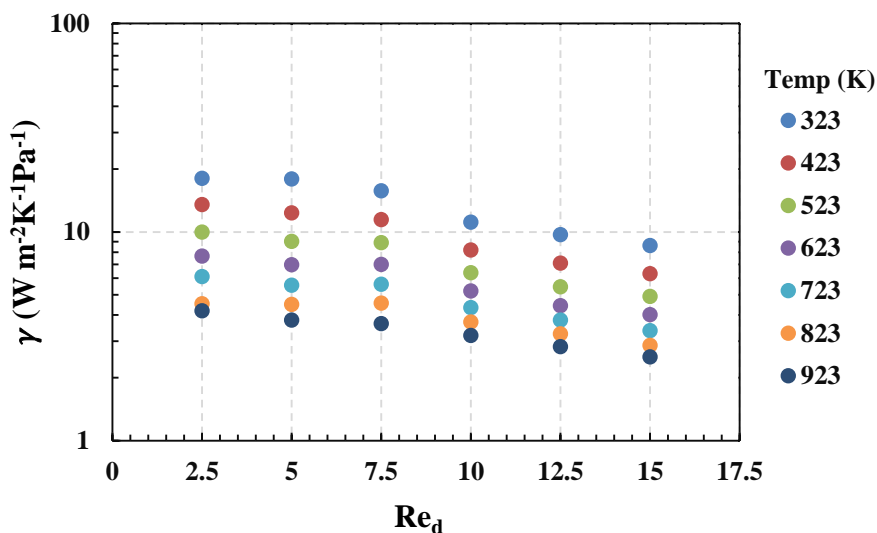
Figure 4.20: Variations of overall heat transfer efficiencies at different temperature of particles.

4.5 Summary

Heat transfer and hydrodynamics inside REVs of packed bed have been studied and analyzed at low Reynolds numbers. The CFD-YADE model adopted to mimic the transport phenomena in the REV has provided reasonable results comparing to those of a digitized image. The closure results were found to be dependent upon the Reynolds number and thermophysical properties of fluid that affect Prandtl number. Moreover, the mean sphere diameter and its local variation analysis inside the bed of spheres revealed no noticeable effect on the results. The generated results will be validated and tested in the next chapter. Finally, CDF-YADE approach can predict relatively reasonable the same output calculated from digitized images or experiments, hence low computational time required and cost differentiates this approach from the others.

Chapter 5

5 Column of Packed Bed of Sand

In this chapter, we solve a one-dimensional case to mimic the experiments described in reference [20] by using a finite-volume model developed on the basis of volume-averaged approach. The code simulates a column of 0.505 m height that has its lower boundary near a heater and air diffuser, and its upper boundary at the exit surface (Fig. 5.1). Air pressures, velocities and temperatures were solved according to the equations described in Chapter 3. The purpose of the coming study is mainly to compare the heat transfer expression proposed in Chapter.4. In this sense, we are not adopting the same assumptions used in analyzing the experiments explained in [20].

5.1 Experimental setup

The closure coefficient of energy equation of packed bed is normally evaluated by applying either a steady state or unsteady state techniques. In the steady case, hot gas flows inside a bed that is kept cool by internal heat exchange and/or by heat removal at the boundary walls. By measuring bed temperatures close to the gas inlet or by measuring temperature gradients in beds containing heaters and coolers, one can find values of h_{fs}.

For the unsteady state method, the temperature of the hot fluid entering is changed in a known manner, the temperature of the exit gas is followed with time, and a heat balance around the bed gives the temperature of the solids at any time, from which and by applying one of the engineering modelling, h_{fs} is found.

In this sense, an experiment comprised of a column of sand has been conducted by [20] to find h_{fs}. In this experiment, an air diffuser and heater element were placed at the bottom of the column, which was subsequently packed with grained silica sand (see Fig. 5.1). Twelve thermocouples were positioned at intervals of 3.5 cm to measure the variation in temperature. The first one is 0.02 m above the heater.

When the experiment commences, the airflow is stagnant and the heater is on at 4.4 A with a standard 120 V AC outlet. The column is heated for approximately 40 minutes; slightly

increasing the temperature at the first thermocouple (x=0.12 m) due to the heat transfer from the heater. The energy is partly stored and partly transferred through the porous medium by conduction. After 30 minutes (t_b), air blower is turned on, and both conduction and convection exist, increasing the temperature due to the convective flux. Once the first thermocouple peaks, the heater is turned off (t_h) 10 minutes after the air diffuser is switched-on. As long there is no more heat input, the stored energy is transferred through the column via the airflow, and the temperature for each thermocouple peaks then, slightly starts to decrease according to different rates based on the location, thus cooling the column down. Note that conduction is dominant when the air blower is not activated, Fig. 5.2, resulting in a higher peak temperature for the first thermocouple at 0.12 m. Once the convection dominates, heat transfer of the stored energy to the upper sand of the column is carried by the induced air thus, heating the upper regions of the column. The heat transfer between the sand and the gas phase is controlled by the heat transfer coefficient, h_{fs}, that was studied in the previous chapter. More information about the experiment setup is provided in reference [20].
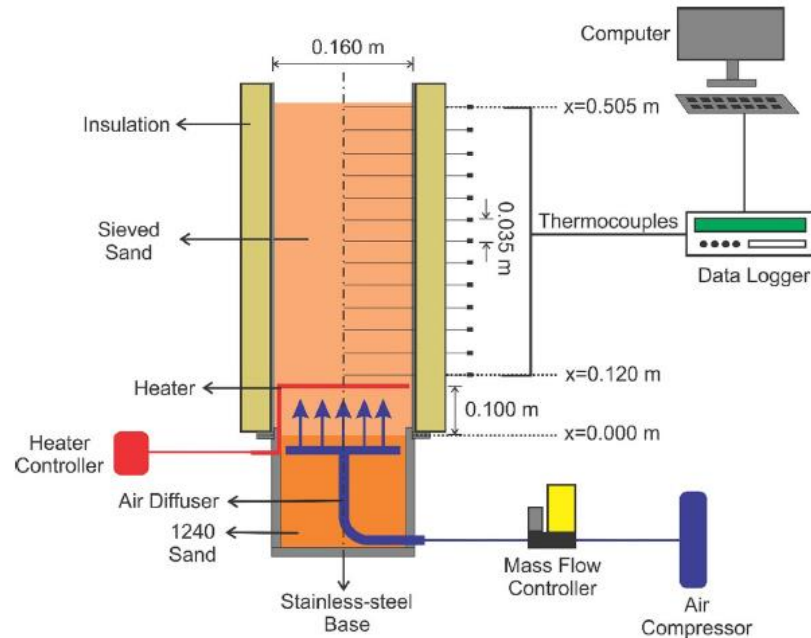
Figure 5.1: Cross section diagram of experimental apparatus [20].
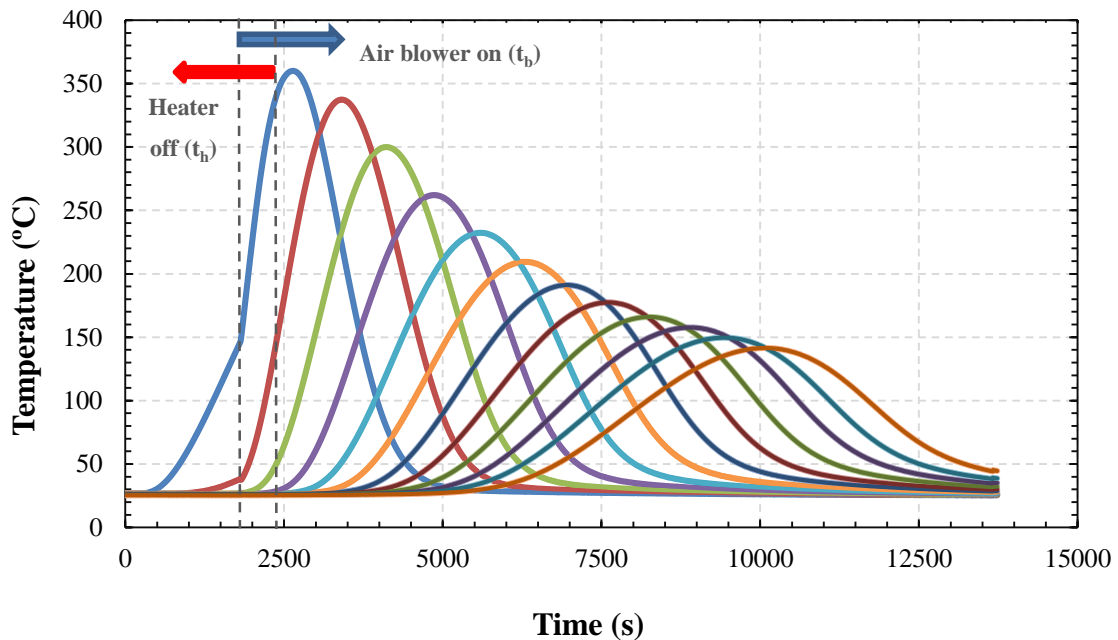
Figure 5.2: Experimental temperature evolution versus time. It shows thermocouple positions (x) from 0.120 to 0.505 m with 0.035 m intervals for 80 L/min [20].

5.2 Numerical modelling

Numerical models are developed by researchers to analyze and understand unexplored physics occurring in the potential models. In engineering field, modelling is divided into experimental modelling and analytical (theoretical) modelling. Laboratory model tests are examples of experimental modelling, from which engineers and scientists obtain useful information to develop empirical relations. On the other hand, theoretical modelling usually consists of multiple steps. The first step is building a mathematical model for corresponding physical problems based on appropriate assumptions of a predefined geometry. The second step is the development of an appropriate numerical model to mimic the mathematical model. The third step of theoretical modelling is the actual implementation of the numerical model to obtain results. Finally, the numerical model needs to be carefully calibrated and validated against pre-existing data and experiential results.

The description of most engineering problems involves identifying key variables and defining how these variables are produced. One of these variables is the interfacial heat transfer coefficient h_{fs} that represents the heat exchange between the interface of the solid and fluid phase. The most common approach for determining h_{fs} is based on experiments, from which empirical correlations are formulated by inverse modelling method. For instance, Wakao and Kaguei [44] have extensively carried out experiments in steady state and transient conditions for different cases in packed beds of spherical particles.

In this work, we will validate the heat transfer expression described in Chapter 4 against the experiment results explained earlier. Concerning this experiment, the initial and boundary conditions referred to in the momentum and energy equations are provided in Table 5.1. At lower inlet, the heater was simulated and adjusted by piecewise functions in order to mimic the real temperature, which follows the experimental procedure discussed in previous part. The inlet pressure is extrapolated from interior fluid to the outside. On the outlet side, the outlet condition assumes zero normal gradients for flow velocity and temperature, and the pressure is ambient pressure. Fluid and solid physical properties are allowed to vary with respect to temperature. Table 5.2 shows the porous media physical properties.

Table 5.1: Initial and boundary conditions for 80 L/min airflow.

Equation	Initial Condition	Position (cm)	Boundary Condition
Momentum	$P = atm$ $U = 0$	$x = 0$	$\dfrac{\partial P_f}{\partial x} = Extrapolate$ $U = U_o \quad t > t_b$
		$x = 0.405$	$P_f = atm$ $\dfrac{\partial U}{\partial x} = 0$
Temperature	$T_s = T_f = 25\,°C$	$x = 0$	$T_s = T_{heater}$ $= \left(\begin{matrix} 600\,°C & 0 \leq t \leq t_h \\ 25\,°C & t_h \leq t \leq t_f \end{matrix} \right)$ $T_f = 25\,°C$
		$x = 0.405$	$\dfrac{\partial T_s}{\partial x} = \dfrac{\partial T_f}{\partial x} = 0$

*Heater time (t_h)=0 to 40 min   Blower time (t_b)=30 to t_f min   Experiment time (t_f)=226 min

The solid matrix is composed of sand, and the fluid phase is assumed air. The simulated model follows the assumptions:

I. The ideal gas law is valid

II. Variable properties with temperature

III. Local thermal non-equilibrium is assumed as explained in Chapter 3 with no heat losses.

IV. The air diffuser is imposed as an inlet velocity boundary condition

V. The heater is analogous to a temperature boundary condition

VI. Radiation heat transfer is valid

Table 5.2: Physical properties applied in the experiment.

Material Properties	Values	Unit	Reference
Permeability (K)	2.263 x 10^{-9}	m^2	Calculated
Sand specific heat capacity (C_{ps})	2.49(T$_s$)+39.06	J/ kg K	[20]
Thermal conductivity – sand (k_s)	0.000541(T$_s$)+0.1044	W/m K	[20]
Thermal conductivity – air (k_f)	Appendix (2)	W/m K	[30]
Density of sand (ρ)	2650	kg/m^3	[30]
Air viscosity (μ)	Appendix (2)	Pa. s	[30]
Specific gas constant for air (R)	287	J/ kg K	-
Specific heat of gas (C_{pg})	Appendix (2)	J/ kg K	[30]
Porosity (ϕ)	37	%	[20]
Heater temperature	600	°C	-
Inlet velocity (U_o)	0.065	m/s	[20]
Particle diameter (d)	1.59 x 10^{-3}	m	[20]

The radiation model herein is based on the solution adopted by Rosseland approximation and is implemented as a radiative conductivity $k_{rad} = 16\sigma d T_s^3/3$ [66]. Note that the viscous dissipation has been neglected in the energy equation. This assumption is certainly reasonable for low Reynolds numbers.

Concerning the closure form, for cold flow and constant thermophysical properties, the coefficients are simply constant and determined based on the fluid type and the geometry of the material. For instance, Wakao et al presents the closure for packed spheres in cold flow as [40,44],

$$\text{Nu} = 2 + 1.1\, Pr^{1/3} Re^{0.6} \qquad (2.3)$$

However, in high temperature flow, additional corrections must be added to account for the strong variations of thermophysical properties that occur across the flow. This is commonly accomplished by introducing another set of empirical factors into the previous equation, usually in the form of a ratio of the property value at free-stream temperature to the same property at the wall (particle surface) temperature raised to some power as shown in Eq. 4.11. The equation coefficients are presented in Table 4.4.

$$Nu = a\frac{k_w}{k_\infty} + bPr_\infty^{1/3}Re_\infty^{0.6}\left(\frac{\rho_\infty\mu_\infty}{\rho_w\mu_w}\right)^c\left(\frac{c_{p\infty}}{c_{pw}}\right)^d \quad Pr = 0.7 \tag{4.11}$$

In terms of other relevant computational details, in the present computational model, the advection scheme in fluid constituent of porous regions was the upwinding scheme (UDS) since the flow has one unidirectional flow field and no added sources. Note that the solution procedure advances forward in time taking five iterations per time-step towards the final solution. The solution is said to be converged when the maximum normalized residual of all the transport equations decreases below 10^{-6}.

After grid-convergence testing, the final grid consists of 40 hexahedral control-volumes in the flow direction. A time-step size of 5s was selected for the current simulations, based on the inlet Reynolds number. Variation of the time-step size from 1, 2, 5 until 50s showed slight change in convergence behaviour but computational time was decreased. Smooth advance can be reached when time-step is less than 10s.

5.3   Results and discussion

In many cases it is a good assumption that the solid and fluid phases are in thermal equilibrium, but there are situations where this is not applicable [9]. It is hard and may be impossible to measure the temperature of each phase separately. Therefore, the non steady transient convection heat transfer problem needs to be analyzed numerically.

From the experiment setup and the output results, it is clear that the heating zone near the heater could not be shown due to the lack of thermocouples. The region of the conduction influence indicates a heated distance 0.12 m thick. When the airflow starts, convective heat transfer of the stored energy along the column ensues, which is shown as a rapid increase

in the temperature of the thermocouples above the heater. After 2400s, the heater is turned off and only the stored energy in the sand remains to be released to the interstitial airstream. The zones near the heater then begin to cool as the air acts as a coolant leading to a noticeable decrease in the temperature. Later, the absorbed heating energy is dissipated into the environment. Figure 5.3 shows the experimental temperature from 0.120 to 0.505 m with 0.035 m intervals. Since it is reported in [20] that the temperature measurements are essentially that of the solid particle phase, we compare herein the experimental temperature results with the solid phase temperature of our numerical results and those of Eq. 2.9. Based on the output result shown in Fig. 5.3(a), the trends of temperature variation with time are accurately predicted, but the predicted solid temperatures are slightly higher than the experimental ones. This over-prediction of solid temperature may be due to differences between the imposed energy input and the heater input in the experiments. On the other hand, Fig. 5.3(b) slightly under-estimated the real energy transferred. This is due to the fixed value of h_{fs} for all the column cells.

a)   b)
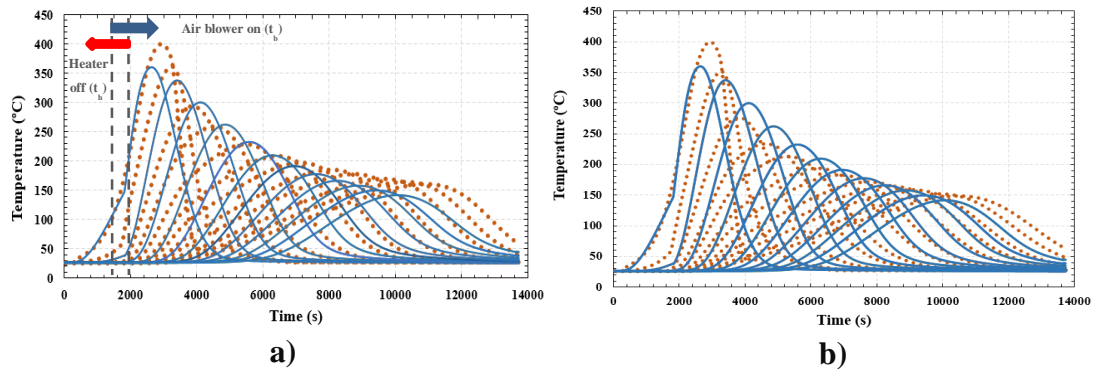
Figure 5.3: Experimental temperature evolution versus time. It shows thermocouple positions (x) from 0.120 to 0.505 m with 0.035 m intervals. The solid curves represent the experiments and the dotted curves represent the numerical results of solid constituent for closures based on a) Eq. 4.11. b) Eq. 2.9. The flow is 80 L/min.

It is also useful to discuss the sand behaviour in different time intervals. This analysis will help in understanding the thermal development inside the packed bed. In Fig. 5.4 and based on the closure derived in Chapter 4, the profiles of temperature are presented where each line represents a different time interval. Results are plotted in approximately 1080 s increments. Initially, the packed bed is at 25°C. As the air is forced up through the bottom

boundary of the column at 0.065 m/s, the heat wave propagates gradually upwards reaching the peak temperature for each selected position, then falls down and this is due to the shut-down of the heater source. It is obvious that the high peak temperature is achieved near the heater and the following trends keep the same behaviour. However, the heat wave keeps losing its peak with time until a straight line remains at the end of the experiment.
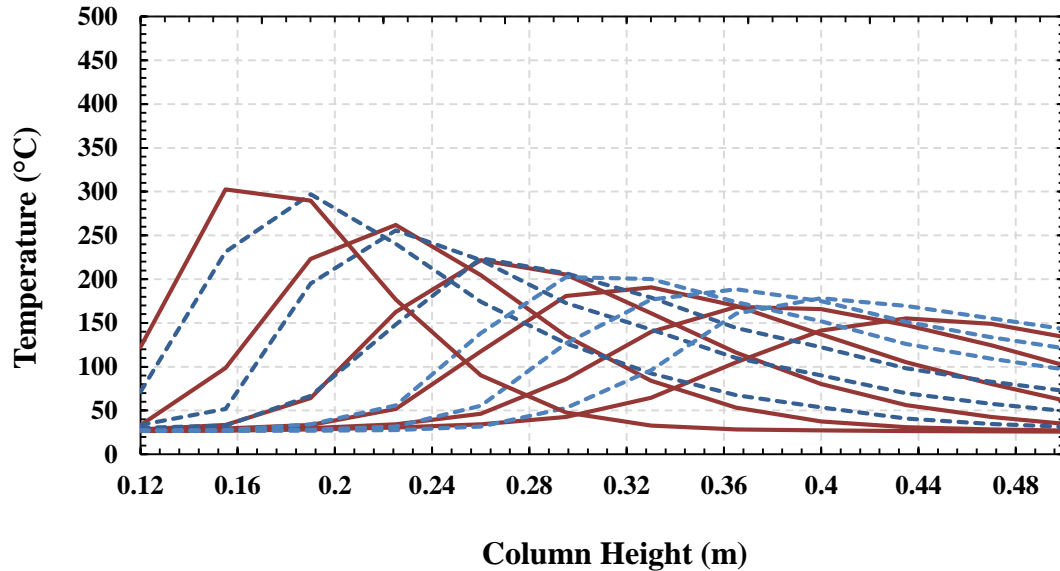
Figure 5.4: Experimental times (t) from 3840 to 9240 s with intervals of 1080 s (temperature profile versus height of the column). Dotted lines represent the numerical results of solid temperature and the solid lines represent the experiments.

5.4 Summary

The previous case investigated numerically studies the development of transient heat transfer model based on the formulation derived in Chapter 3. We presented the numerical results of the solid phase against the experimental ones [20] as it was relatively able to simulate the transport effect in the packed bed of sand. The correlation derived from YADE model for the case studied overestimated the heat transfer relation of the modelling process in the packed bed. The correlation derived in [20] showed reasonable outputs due to the assumption of heat loss. Such detailed modeling enabled us to understand certain details of the heating and cooling process in each cell with respect to time and space.

Chapter 6

6 Summary

This chapter summarizes the work conducted for this thesis, outlines the research contributions, and suggests future avenues of investigation for extending the present study.

6.1 Conclusion

As explained in previous chapters, the primary achievement of the research presented in this thesis is the development of a simple pore-level geometric model that can be used for establishing closure models for a porous continuum approach. An additional accomplishment is the subsequent determination of the influence of particle size variation and the influence of temperature-varying properties on the heat transfer and flow behavior in a representative elemental volume (REV) of a packed bed of sand particles. Due to the importance of heat transfer closure coefficients with respect to the packed bed model, considerable effort was devoted to the evaluation of these parameters. Most of the correlations reported in the studies published in the literature are valid only for high Reynolds numbers. Because these correlations are applicable only for the experimental conditions for which they were developed, extrapolations for other specific conditions may result in improper modelling of the system under study.

Chapter 4 described the formulation of a computational analysis capable of simulating a pore-level scale for packed beds of sand. Governing transport equations were described specifically for the fluid component. The closure results were found to be dependent on the Reynolds number and on the particle surface temperature, which affects the thermophysical properties of the fluid. The developed model was first validated based on a comparison of the results against those of the digitized image of a packed bed of sand. Another simulated case demonstrated that the findings were reasonable compared to available experimental results and that they were physically realistic.

Chapter 5 explained how the formulation derived in Chapter 3 was employed for simulating a column of a packed bed of sand. The column of sand was considered to be a porous continuum that was modelled in one dimension. The model adopted the non-equilibrium

heat transfer assumption in the porous region such that the physical relation between the fluid and solid constituents could be captured. Achieving an accurate representation of the complexity of the transient problem necessitated that the existence of the interfacial heat transfer between the porous phases. A further element of this study was a comparison of the results from the developed model based on the calculated correlation against the available one derived from experimental temperature data. It was concluded that the current model slightly over-predicted the thermal behaviour of the system versus time and space.

6.2 Contribution

Chapter 4 outlined the development of a simple pore-level geometric model that can be used for calculating the coefficients of closure forms of the volume-averaged equations, which constitutes the main contribution of the research presented in this thesis. The calculation of the coefficients for packed beds of spheres at a low Reynolds number represents a further enhancement. Thus, the closure forms were derived for the volume-averaged model based on the output of the CFD-YADE simulations.

The calculation of such detailed closures constituted a necessary step in the closing of the volume-averaged equations of a macroscopic model. No previous studies have been focused on such detailed three-dimensional closures. The existing literature also lacks the detailed information that was acquired during the present work in order to derive the closures. Moreover, a parametric study was employed, which revealed that for a specific mean sphere diameter, local variations inside a bed of spheres have an insignificant effect on the results, and the closure results were found to be sensitive to the temperature variation inside the REV. As a result, the impact of temperature variation on the thermophysical properties of fluid influences Prandtl number.

A second accomplishment was the detailed modelling of packed bed of sand, which was described in Chapter 5. This work included the modelling of a column of sand as a porous continuum based on detailed information about the thermophysical properties of both the fluid and solid constituents. The transient air flow was simulated in conjunction with the derived correlation. Such detailed modelling of the packed bed of sand enabled the capture of details related to the heating and cooling process in each cell with respect to time and

space, the differences between experimental and numerical results, and the relation between the porous constituents that is governed by the interfacial heat transfer.

6.3 Future work

In Chapter 4, it was noticed that the shape of spherical particles could simulate the geometry of sand. However, at very low Reynolds number, especially near one, the result difference between the scanned image and YADE model is noticeable. A modified shape such as ellipse could therefore mimic the real shape of sand and thus generate more realistic results, but the relation between the minor and major radius of an ellipse should first be defined without modifications to the porosity of the REV and its particle volume. For this reason, the ImageJ software fit option was applied because it returns the semi-major and semi-minor axis for each ellipse for all images. The results are shown in Appendix (C). It was found that, for selected images, the ratio of the average semi-major to the semi-minor is 1.45. This result will be used for generating an ellipse that measures 1.45 in z direction multiplied by any of x- y directions. It should be noted that the range of particle diameters for the scanned image is 420 to 600, which represents a ratio of 1.428 between the two limits.

Since the particle volume is conserved, calculating the major and the minor diameters is straightforward. The new measurement is (450 μ m) for x- y directions and (652 μ m) for z direction. It is important to mention that for Reynolds number calculation, the characteristic diameter is defined as the average of all shape diameters. Figure 6.1 suggests two strategies for building REV composed of ellipses: clumps of particles or elliptical particles. Figure 6.2 shows the final geometry of elliptical particles generated in Autodesk Inventor™ [67].

Based on the simulation results for both the spherical (presented in Chapter 4) and elliptical cases, which are shown in Fig. 6.3 and Fig. 6.4, it is obvious that the Nusselt number of ellipse shape exhibits better agreement with the image results, an effect that is attributable mainly to the more accurate interfacial surface area in this case. The addition of more surface area would enhance the heat transfer process. It was observed that the REV based on the ellipse has a surface area relatively closer to that in the image.

a)   b)
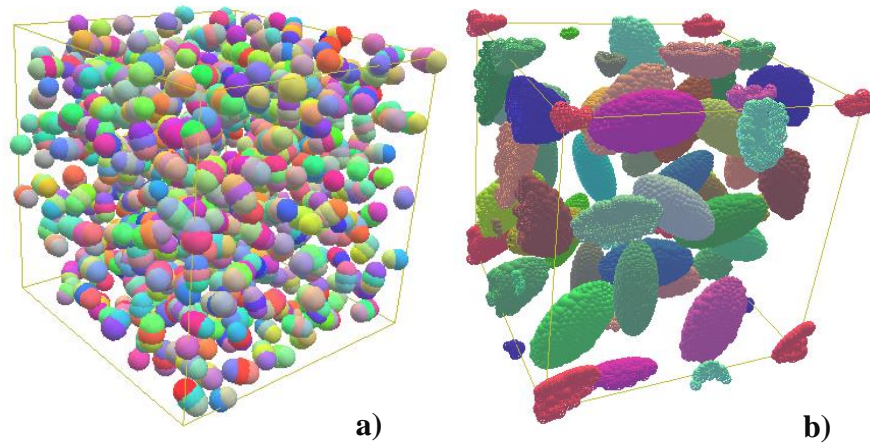
Figure 6.1: YADE REV composed of (a) Clumps model of particles. (b) Ellipses.

3.2 mm
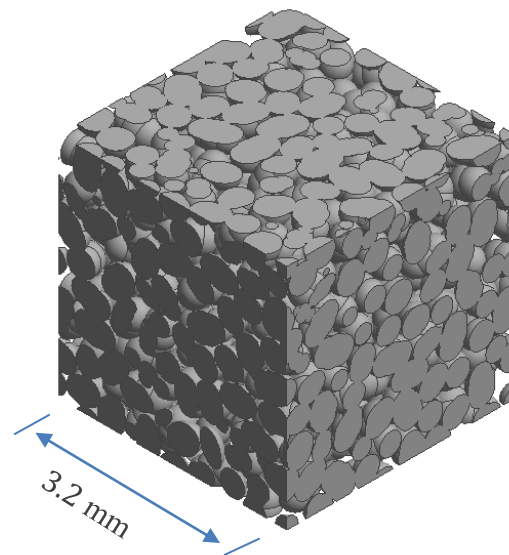
Figure 6.2: REV of elliptical shape generated in Autodesk Inventor™. The REV has the same porosity as the digitized image of sand.

When the spherical shape was compared with the digitized image, the deviations in the heat transfer results ranged from 23.19 % at a low Reynolds number to 3.44 % at a high value (Chapter 4), whereas for the elliptical shape, the results' deviations were 16 % to
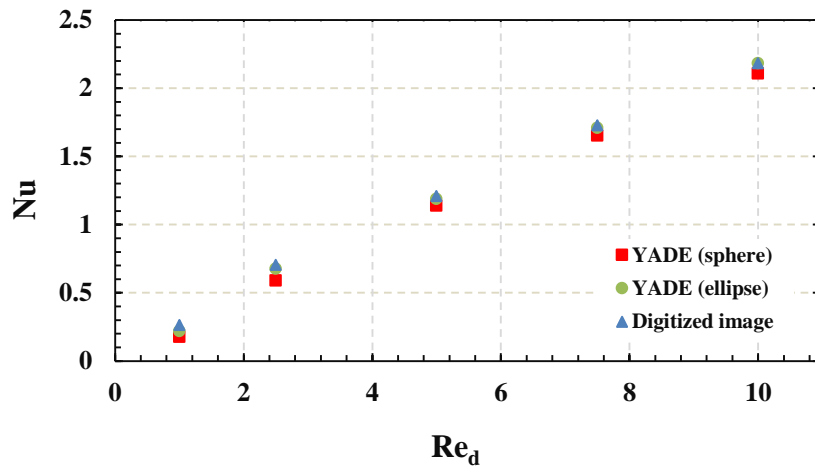
Figure 6.3: Comparison between REVs based on Nusselt number as a function of Reynolds number for different shapes (Sphere, ellipse and digitized image). Spherical and elliptical REVs are generated by YADE.

1.1 %, respectively. On the other hand, the pressure drop with the elliptical shape indicated greater resistance to the air flow.This finding may result from the air velocity profile and the greater tortuosity, which would lead to a larger pressure drop. The long paths through which the air must pass allow the build-up of thicker boundary layers, in contrast to the shorter paths associated with a spherical shape.
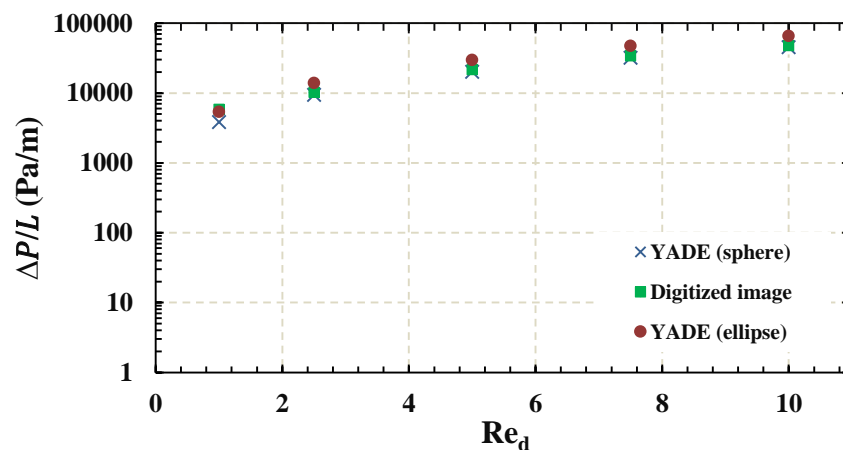
Figure 6.4: Comparison between REVs based on Pressure drop through the length (L) of the REV.

6.3.1   Recommendations for further investigation

As an extension of the work presented in this thesis, the following recommendations are presented for consideration:

I.   In addition to spheres and ellipses, combinations of more complicated shapes such as polyhedrons, with different ranges of particle variation, might mimic the real shapes of sand, as illustrated in Fig. 6.5. The formulation of a robust relation that links real sand dimensions with those of the shapes generated could be undertaken.
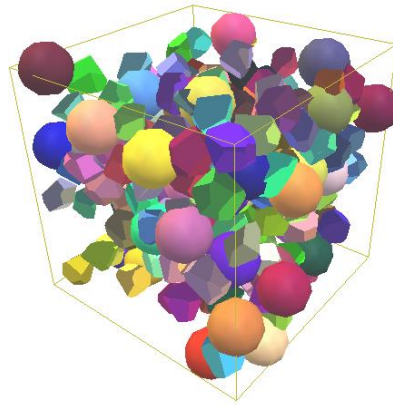
Figure 6.5: REV composed of particles of polyhedrons and spheres.

II.   For the simulations performed in this research, the heat transfer closure was generated based on the heating of the solid constituent. Including consideration of closure based on a cooling effect could enhance the final results.

III.   With respect to the extension of the column model introduced in Chapter 5, an appropriate next step would be to simulate the complete column in three dimensions. Such a complete analysis might help enhance the understanding of heat transfer in the radial direction, especially at a large scale. This extended investigation could enable the capture of the numerous processes that occur inside a packed bed, especially with respect to local radial heat loss.

References

[1] Khan, F. A., Fischer, C., and Straatman, A. G., 2015, "Numerical Model for Non-Equilibrium Heat and Mass Exchange in Conjugate Fluid/solid/porous Domains with Application to Evaporative Cooling and Drying," Int. J. Heat Mass Transf., 80, pp. 513–528.

[2] Schlichting, H., 1979, Boundary-Layer Theory, McGraw-Hill.

[3] Cunningham, R. E., Williams, R. J. J., 1980, Diffusion in Gases and Porous Media, Plenum Press, New York.

[4] Kaviany, M., 1995, Principles of Heat Transfer in Porous Media, Springer, New York, NY, 2nd ed.

[5] Forchheimer, P. H., 1901, "Wasserbewegung Durch Boden," Zeitz. Ver. Duetch Ing., 45, pp. 1782–1788.

[6] Ergun, S., 1952, "Fluid Flow through Packed Columns.," Chem. Eng. Prog., 48, pp. 89–94.

[7] Vafai, K., 2015, Handbook of Porous Media, Boca Raton.

[8] Taylor, G. I., 1953, "Dispersion of Soluble Matter in Solvent Flowing Slowly Through a Tube," Proc. R. Soc. London A Math. Phys. Eng. Sci., 219(1137), pp. 186–203.

[9] Nield, D. A., Bejan, A., 2017, Convection in Porous Media, springer, New York, 5th ed.

[10] Defay, R., Bellemans, A., and Prigogine, I., 1966, Surface Tension and Adsorption.

[11] Weekman, V. W., and Meyers, J. E., 1965, "Heat Transfer Characteristics of Cocurrent Gas–Liquid Flow in Packed Beds," AIChE J., 11, pp. 13–17.

[12] Beavers, G. S., and Joseph, D. D., 1967, "Boundary Conditions at a Naturally Permeable Wall," J. fluid Mech., 30(1), pp. 197–207.

[13] Whitaker, S., 1997, "Volume Averaging of Transport Equations," Fluid Transport in Porous Media, Springer, Southampton, UK, pp. 1–59.

[14] Rein, G., 2009, "Smouldering Combustion Phenomena in Science and Technology," Int. Rev. Chem. Eng., 1, pp. 3–18.

[15] "Natural Resources Canada" [Online]. Available: http://www.nrcan.gc.ca/forests/fire-%0Ainsects-disturbances/fire/13143%0A. [Accessed: 10-May-2017].

[16] "Savron Smoldering Solutions" [Online]. Available: http://www.savronsolutions.com. [Accessed: 30-May-2017].

[17] Whitaker, S., 1996, "The Forchheimer Equation: A Theoretical Development," Transp. Porous Media, 25(1), pp. 27–61.

[18] Vafai, K., and Tien, C. L., 1981, "Boundary and Inertia Effects on Flow and Heat Transfer in Porous Media," Int. J. Heat Mass Transf., 24(2), pp. 195–203.

[19]   Molnar, I. L., 2015, "Silver Nanoparticle Transport Through Soil: Illuminating the Governing Pore-Scale Processes," PhD Thesis, Western University. Electronic Thesis and Dissertation Repository. 3394. http://ir.lib.uwo.ca/etd/3394.

[20]   Zanoni, M. A. B., Torero, J. L., and Gerhard, J. I., 2017, "Determination of the Interfacial Heat Transfer Coefficient between Forced Air and Sand at Reynold's Numbers Relevant to Smouldering Combustion," Int. J. Heat Mass Transf., 114, pp. 90–104.

[21]   Dyck, N. J., and Straatman, A. G., 2015, "A New Approach to Digital Generation of Spherical Void Phase Porous Media Microstructures," Int. J. Heat Mass Transf., 81, pp. 470–477.

[22]   Leach, S. V., Rein, G., Ellzey, J. L., Ezekoye, O. A., and Torero, J. L., 2000, "Kinetic and Fuel Property Effects on Forward Smoldering Combustion," Combust. Flame, 120(3), pp. 346–358.

[23]   Schult, D. A., Matkowsky, B. J., Volpert, V. A., and Fernandez-Pello, A. C., 1996, "Forced Forward Smolder Combustion," Combust. Flame, 104(1), pp. 1–26.

[24]   Hurley, M., 2016, SFPE Handbook of Fire Protection Engineering, Springer, New York.

[25]   Summerfield, M., Ohlemiller, T. J., and Sandusky, H. W., 1978, "A Thermophysical Mathematical Model of Steady-Draw Smoking and Predictions of Overall Cigarette Behaviour," Combust. Flame, 33, pp. 263–279.

[26]   Fatehi, M., and Kaviany, M., 1994, "Adiabatic Reverse Combustion in a Packed Bed," Combust Flame, 99(1), pp. 1–17.

[27]   Chen, H., Rien, G., and Liu, N., 2015, "Numerical Investigation of Downward Smouldering Combustion in an Organic Soil Column," Int. J. Heat Mass Transf., 84, pp. 253–261.

[28]   Fang, H., NicO, Z., Wenjian, Z., and Frank, B., 2009, "Effects of Physical Properties on One-Dimensional Downward Smouldering of char:Numerical Analysis," Biomass and Bioenergy, 33(8), pp. 1019–1029.

[29]   Rein, G., Fernandez-Pello, C., and Urban, D., 2007, "Computational Model of Forward and Opposed Smoldering Combustion in Microgravity," Proc. comdustion Institute., 31, p. 2677–2684.

[30]   Incropera, F., Dewitt, D., Bergman, T., and Lavine, A., Fundamentals of Heat and Mass Transfer, Wiley, Hoboken, NJ. 5th ed.

[31]   Bear, J., 1988, Dynamics of Fluids in Porous Media, Dover.

[32]   Ward, J. C., 1964, "Turbulent Flow in Porous Media," J. Hydraul. Div. Proc. Am. Soc. Civ. Eng., 90(5), pp. 1–12.

[33]   Whitaker, S., 1967, "Diffusion and Dispersion in Porous Media," A.I.Ch.E. J., 13(3), pp. 420–427.

[34]   Slattery, J. C., 1967, "Flow of Viscoelastic Fluids through Porous Media," A.I.Ch.E. J., 13(6), pp. 1066–1071.

[35] Khan, F. A., and Straatman, A. G., 2016, "Closure of a Macroscopic Turbulence and Non- Equilibrium Turbulent Heat and Mass Transfer Model for a Porous Media Comprised of Randomly Packed Spheres," Int. J. Heat Mass Transf., 101, pp. 1003–1015.

[36] Yu, Q., Thompson, B. E., and Straatman, A. G., 2006, "A Unit Cube-Based Model for Heat Transfer and Fluid Flow in Porous Carbon Foam," J. Heat Transfer, 128(4), pp. 352–360.

[37] Karimian, S. M., and Straatman, A. G., 2008, "CFD Study of the Hydraulic and Thermal Behavior of Spherical-Void-Phase Porous Materials.," Int. J. Heat Fluid Flow, 29(1), p. 292–305.

[38] Yang, J., Wang, Q., Zeng, M., and Nakayama, A., 2010, "Computational Study of Forced Convective Heat Transfer in Structured Packed Beds with Spherical or Ellipsoidal Particles.," Chem. Eng. Sci., 65(2), pp. 726–738.

[39] Yang, J., Wang, J., Bu, S., Zeng, M., Wang, Q., and Nakayama, A., 2012, "Experimental Analysis of Forced Convective Heat Transfer in Novel Structured Packed Beds of Particles," Chem. Eng. Sci, 71, pp. 126–137.

[40] Wakao, N., Kaguei, S., and Funazkri, T., 1979, "Effect of Fluid Dispersion Coefficients on Particle-to-Fluid Heat Transfer Coefficients in Packed Beds: Correlation of Nusselt Numbers," Chem. Eng. Sci, 34 (3), pp. 325–336.

[41] Kar, K., and Dybbs, A., 1982, "Internal Heat Transfer Coefficient of Porous Metals," NASA STI/Recon Tech. Rep. A, 84, pp. 81–91.

[42] Kamiuto, K., and Yee, S., 2005, "Heat Transfer Correlations for Open-Cellular Porous Materials," Int. Commun. Heat Mass Transf., 32 (7), p. 947–953.

[43] Nakayama, A., Ando, K., Yang, C., Sano, Y., Kuwahara, F., and Liu, J., 2009, "A Study on Interstitial Heat Transfer in Consolidated and Unconsolidated Porous Media," Heat Mass Transf., 45 (11), pp. 1365–1372.

[44] Wakao, N., Kaguei, S., 1982, Heat and MassTransferinPackedBeds, McGraw-Hill, NewYork.

[45] Kunni, D., and Levenspiel, O., 1991, Fluidization Engineering, Reed Publishing, Butterworth. 2ed.

[46] Kothari, A., 1967, "M.S. Thesis," Illinois Institute of Technology, Chicago.

[47] Betchen, L. J., Straatman, A. G., and Thompson, B. E., 2006, "A Nonequilibrium Finite-Volume Model for Conjugate Fluid/solid/porous Domains," Numer. Heat Transf., Part A, 49, pp. 543–565.

[48] Whitaker, S., 1998, "Coupled Transport in Multiphase Systems: A Theory of Drying," Adv. heat Transf., 31, pp. 1–104.

[49] Ferreira, J.A., Barbeiro, S., Pena, G., and Wheeler, M., 2013, Modelling and Simulationin of Fluid Dynamics in Porous Media, Springer, London.

[50] Šmilauer, V., and Chareyre, B., 2011, Yade Documentation.

[51]   Cundall, P. A., and Strack, O. D., 1979, "A Discrete Numerical Model for Granular Assemblies.," Geotechnique, 29(1), pp. 47–65.

[52]   Dassault Systemes, Solidworks Educational Version 2015-2016.

[53]   ANSYS, Workbench Meshing Tool, vol.16.0.

[54]   ANSYS, ANSYS CFX vol.16.0.

[55]   ANSYS, Fluent vol.16.0.

[56]   ANSYS Fluent Theory Guide, Release 16.0.

[57]   ANSYS CFX-Pre User's Guide, Release 16.0.

[58]   Molnar, I. L., Gerhard, J. I., Willson, C. S., and O'Carroll, D. M., 2015, "The Impact of Immobile Zones on the Transport and Retention of Nanoparticles in Porous Media," Water Resour. Res., 51(11), pp. 8973–8994.

[59]   Molnar, I. L., Sanematsu, P. C., Gerhard, J. I., Willson, C. S., and O'Carroll, D. M., 2016, "Quantified Pore-Scale Nanoparticle Transport in Porous Media and the Implications for Colloid Filtration Theory," Langmuir, 32(31), pp. 7841–7853.

[60]   Rivers, M. L., Citron, D. T., and Wang, Y., 2010, "Recent Developments in Computed Tomography at GSECARS.," Proc. SPIE, Dev. X-Ray Tomogr. VII, 7804, p. 780409.

[61]   ANSYS ICEM CFD User's Manual, Release 16.0.

[62]   Trevisan, O. V., and Bejan, A., 1985, "Natural Convection with Combined Heat and Mass Transfer Buoyancy Effects in a Porous Medium," Int. J. Heat Mass Transf., 28(8), pp. 1597–1611.

[63]   Zellnik, H., and Churchill, S., 1958, Convective Heat Transfer from High-Temperature Air Inside a Tube, University of Michigan, MI, USA.

[64]   Humble, L. V., Lowdermilk, W. H., and Desmon, L. G., 1951, "Measurements of Average Heat-Transfer and Friction Coefficients for Subsonic Flow of Air in Smooth Tubes at High Surface and Fluid Temperatures."

[65]   Young, R. M., and Pfender, E., 1987, "Nusselt Number Correlations for Heat Transfer to Small Spheres in Thermal Plasma Flows. Plasma Chemistry and Plasma Processing," 7(2), pp. 211–229.

[66]   Rosseland, S., 1931, Astrophysik Aud Atom-Theoretische Grundlagen, Springer, Berlin.

[67]   Autodesk Systemes, Inventor Educational Version 2014-2015.

[68]   Çengel.Y. A. and Ghajar. J., Heat and Mass Transfer. Fundamentals and Applications, New York, NY. 5th ed.

Appendix A: Derivation of the interfacial heat transfer closure

Based on the first law of thermodynamics and for a control volume, the energy equation could be written as, (the following formulas are derived based on the author understanding of heat transfer phenomena). The main heat transfer references used herein are [30,68].

$$\frac{dE_{stored}}{dt} = \dot{E}_{in} - \dot{E}_{out} + \dot{E}_{generated}$$

After few simplifications, also neglecting viscous dissipation and conduction in axial direction,

$$\dot{m}\left(u_t + pv + V^2/2 + gz\right)_{in} - \dot{m}\left(u_t + pv + V^2/2 + gz\right)_{out} + q - \dot{W} = 0$$

The enthalpy is defined as,

$$i = u_t + pv$$

For ideal gas and assuming constant specific heats, the enthalpy difference is,

$$i_{in} - i_{out} = c_p(T_{in} - T_{out})$$

Assuming steady-state conditions, no change in thermal or mechanical energy generation, neglecting kinetic and potential energy changes and flow work, then the simplified steady-state equation:

$$q = \dot{m}c_p(T_{out} - T_{in})$$

An energy balance could be applied to determine how the mean temperature $T_m(x)$ varies with position along the surface and how the total convection heat transfer q is related to the difference in temperatures at the geometry inlet and outlet. The derived expression applies no matter the nature of the surface thermal or flow conditions.

$$q = \dot{m}c_p(T_{m,out} - T_{m,in})$$

$$dq_{conv} = \dot{m}c_p[(T_m + dT_m) - T_m]$$

$$dq_{conv} = \dot{m}c_p dT_m$$

This equation may be cast as,

$$dq_{conv} = q_s'' P dx$$

where P is the surface perimeter of the studied surface. Newton's law of cooling is,

$$q_s'' = h(T_s - T_m)$$

where h is the local convection heat transfer coefficient, T_s is the surface temperature, and T_m is the mean temperature. Based on the previous assumption, final expression is,

$$\frac{dT_m}{dx} = \frac{q_s'' P}{\dot{m}c_p} = \frac{P}{\dot{m}c_p} h(T_s - T_m)$$

Define that $\Delta T = (T_s - T_m)$, and then integrate along the surface length L,

$$\frac{dT_m}{dx} = -\frac{d(\Delta T)}{dx} = \frac{P}{\dot{m}c_p} h \Delta T$$

Separating Variables and integrating,

$$\int_{\Delta T_i}^{\Delta T_o} \frac{d(\Delta T)}{\Delta T} = -\frac{P}{\dot{m}c_p} h \int_0^L dx$$

$$\ln \frac{\Delta T_o}{\Delta T_i} = -\frac{PL}{\dot{m}c_p} \left(\frac{1}{L} \int_0^L h \, dx \right) = -\frac{PL}{\dot{m}c_p} \bar{h}$$

$\bar{h}$ is the average convection heat transfer coefficient. Assume surface area is $A = PL$,

$$\ln \frac{\Delta T_o}{\Delta T_i} = \ln \frac{T_s - T_{m,o}}{T_s - T_{m,i}} = -\frac{A}{\dot{m}c_p} \bar{h}$$

$$\bar{h} = -\frac{\dot{m}c_p}{A} \ln \frac{T_s - T_{m,o}}{T_s - T_{m,i}}$$

Appendix B: Air property versus temperature variation (K)

a- Thermal conductivity (K)

W/m.K (10^3)

b- Viscosity (μ)

N.s/m^2 (10^7)

c- Specific heat (Cp)

kJ/kg.K

Temperature (K)
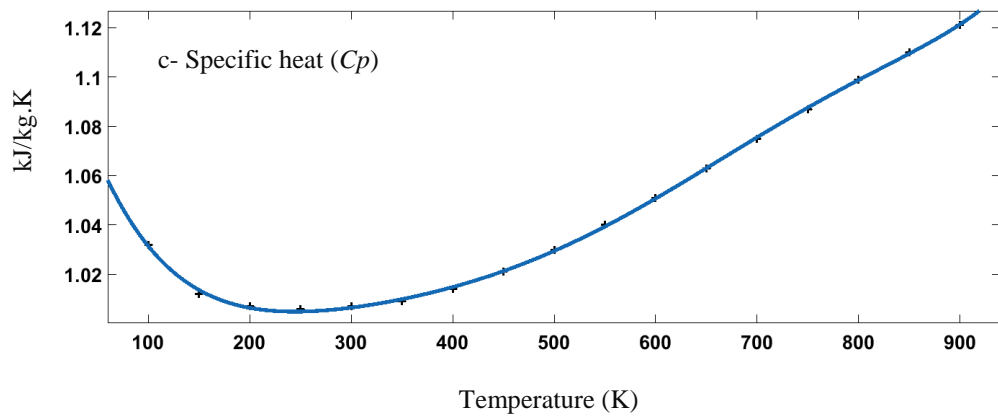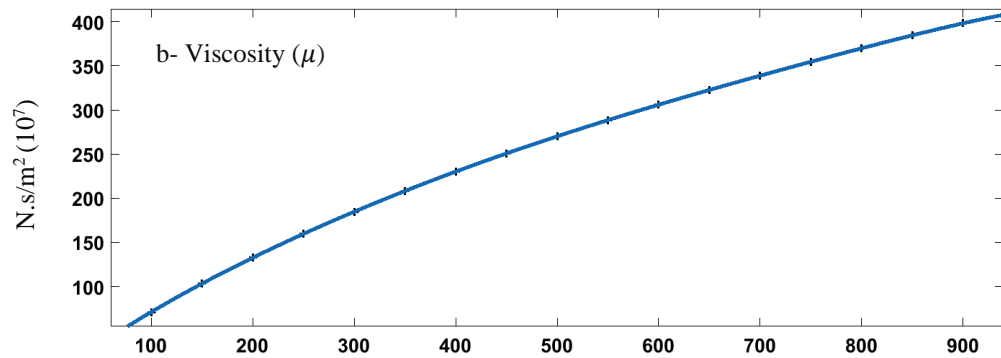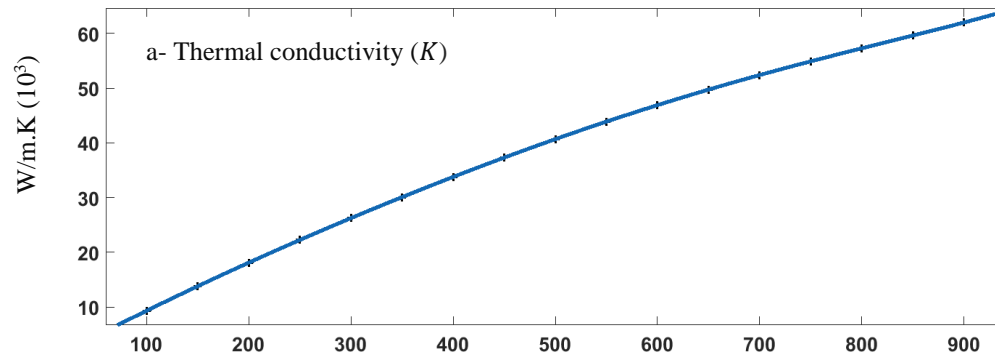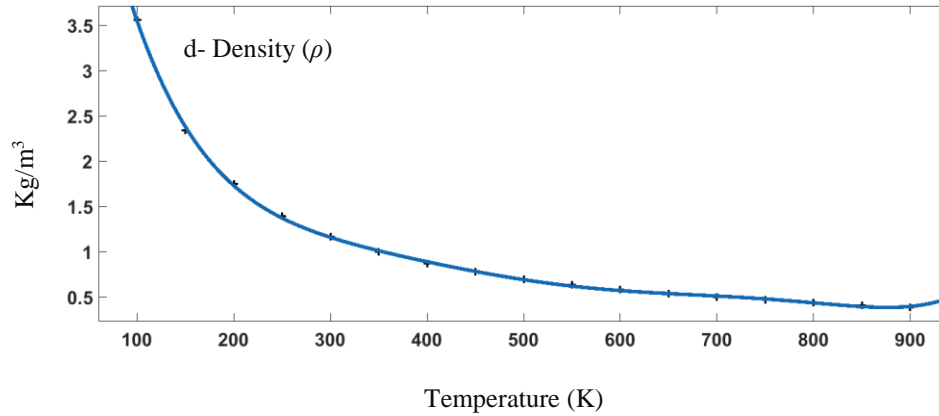
The final correlations are based on six-degree polynomial equations. The black points represent the imported data and the blue curves are the correlated equations. The general form of the applied equation is as follows,

Property= P1*TEMP^6 + P2*TEMP^5 + P3*TEMP^4 + P4*TEMP^3 + P5*TEMP^2 + P6*TEMP + P7

Air Property	*Cp*	*K*	*μ*	*ρ*
P1	9.62e-18	7.574e-17	-1.162e-15	3.058e-16
P2	-3.07e-14	-1.46e-13	3.384e-12	-1.04e-12
P3	3.878e-11	8.725e-11	-3.979e-09	1.428e-09
P4	-2.501e-08	-1.107e-08	2.619e-06	-1.016e-06
P5	9.036e-06	-3.701e-05	-0.001312	0.0003993
P6	-0.001703	0.09884	0.8747	-0.08518
P7	1.133	-0.1773	-5.459	8.951

Appendix C: Geometric properties of the digitized image

The following table is the output information for the 450 voxels of the scanned image. The information includes slice numbers, number of particles, total area of particles, the area percentage, the mean diameters, total major and minor diameters in each slice, and additional data. More information about the software capability is found in (http://imagej.net/).

The ImageJ software fit option that returns the semi-major and semi-minor axis for an ellipse drawn around any closed curve for all images was used and the output results are presented in following table. It was found that the percentage of average semi-major to the semi-minor for selected images is 1.45.

Slice	Count	Total area	Average size	Area %	Mean	Mode	Perim	Major	Minor	Angle	IntDen	Median	Skew
1	10	38054	3805.4	31.064	50.878	46.5	448.124	0.32976	0.26257	61.789	133648.4	49.9	0.341
2	12	37355	3112.917	30.494	51.838	46.25	415.389	0.24993	0.21095	87.78	109334.5	51.75	0.303
3	11	36768	3342.545	30.015	48.373	41.727	519.788	0.35391	0.24034	88.097	117596.3	48.091	0.249
4	7	36422	5203.143	29.732	47.001	45.571	754.897	0.41057	0.34023	93.223	184171.4	46.143	0.433
5	15	36198	2413.2	29.549	51.121	47.2	336.394	0.27004	0.1879	54.586	84954.13	50.733	0.273
6	12	36085	3007.083	29.457	46.857	43.5	406.085	0.32939	0.2295	94.044	106129.3	46	0.441
7	15	36260	2417.333	29.6	50.421	45.667	330.581	0.2833	0.19375	69.756	85072.67	50.133	0.39
8	15	36575	2438.333	29.857	47.837	42.067	374.512	0.24129	0.18889	79.926	85883.67	46.867	0.344
9	14	37141	2652.929	30.319	46.607	39.643	336.569	0.27062	0.20295	81.956	93151.79	44.571	0.567
10	15	37633	2508.867	30.721	46.582	41.667	385.769	0.27589	0.20212	91.786	87893.07	44.667	0.627
11	12	38471	3205.917	31.405	44.794	37.083	311.461	0.32081	0.24812	94.88	112036.6	42.917	0.524
12	15	39190	2612.667	31.992	47.633	45.333	328.142	0.26346	0.20432	75.384	90373.73	46.4	0.447
13	17	39861	2344.765	32.54	45.855	41.412	273.748	0.30518	0.2002	81.678	81025.71	44.353	0.408
14	15	40352	2690.133	32.94	47.994	42.933	353.803	0.35124	0.21709	71.503	92620.07	46.8	0.322
15	15	40683	2712.2	33.211	52.392	50.4	330.893	0.3075	0.19857	77.921	93686.27	51.667	0.345
16	16	41044	2565.25	33.505	53.617	49.688	264.851	0.24142	0.18579	94.905	88300.44	53.188	-0.045
17	19	41101	2163.211	33.552	51.467	47.105	231.622	0.26234	0.16699	86.042	74724.95	50.632	0.42
18	14	41172	2940.857	33.61	50.261	47.929	381.796	0.32117	0.2056	88.437	101417.1	49.786	0.185
19	12	40906	3408.833	33.393	50.612	51.5	470.551	0.36391	0.23533	69.385	117710.9	50.917	0.255
20	12	40747	3395.583	33.263	48.726	45.167	499.986	0.46815	0.26368	65.007	117555.4	47.833	0.424
21	13	40612	3124	33.153	50.198	47.923	410.097	0.43323	0.23943	61.281	108670.2	49.692	0.475
22	16	40177	2511.062	32.798	48.565	45.188	293.896	0.40988	0.23651	78.62	87285.25	47.875	0.371
23	13	40198	3092.154	32.815	49.155	44.538	344.55	0.4305	0.26975	54.144	107165.7	48.462	0.503
24	13	40341	3103.154	32.931	49.059	46.462	396.823	0.42463	0.25549	70.312	107829.7	48.462	0.337
25	11	40376	3670.545	32.96	48.872	44	425.348	0.39444	0.26201	61.182	127119.1	48.545	0.345
26	14	40501	2892.929	33.062	51.259	47.5	331.606	0.29415	0.20387	74.778	100173.7	51.357	0.321
27	11	40430	3675.455	33.004	50.253	45.091	392.333	0.29768	0.23909	87.773	127324.5	49.182	0.145

Curriculum Vitae

Name:	Ashraf Thabet
Post-secondary Education and Degrees:	Concordia University Montreal, Quebec, Canada 2010-2013 M.Eng. The University of Western Ontario London, Ontario, Canada 2015-2017 M.Sc.
Honours and Awards:	Province of Ontario Graduate Scholarship 2015-2016, 2016-2017 Golden Key International Honor Society 2011-2012
Related Work Experience	Teaching Assistant The University of Western Ontario 2015-2017 Graduate Research Assistant The University of Western Ontario 2015-2017